



UNIVERSITAT DE LES ILLES BALEARS
DEPARTAMENT DE FÍSICA

Polarization and Intensity Noise in Vertical-Cavity Surface-Emitting Lasers

*Memoria d'investigació presentada
per Josep Mulet Pol, en el Departament
de Física de la UIB, Octubre
2001.*

Aquesta memòria d'investigació ha estat dirigida pels Doctors *Maxi San Miguel* i *Claudio R. Mirasso* del Departament de Física de la UIB.

Electronic version is available at
<http://www.imedea.uib.es/PhysDept/publications/>

Contents

Resum - Outline	ix
1 Introduction	1
1.1 A brief history about lasers	1
1.2 Semiconductor lasers	2
1.3 Surface-emitting semiconductor lasers	5
2 Fundamentals of the VCSEL Modeling	9
2.1 Quantum Noise	9
2.2 Polarization Dynamics	12
2.3 Linearly-Polarized Solutions	19
2.4 Linearized Spin Flip Model	20
3 Semiclassical Analysis of Fluctuations	23
3.1 Introduction	23
3.2 Regimes of Operation	25
3.3 Fluctuation of the Intensity Components	31
3.4 Fluctuation of the Polarization Angles	37
3.5 Role of the Spin Flip and Birefringence	41
3.6 Polarization Anticorrelations	44
4 Summary, Discussion and Perspectives	47
Appendix A: Definitions	51
Appendix B: Itô Transformation	53
Bibliography	55
Curriculum vitae	60

List of Figures

1.1	Sketch of an edge-emitting semiconductor laser	3
1.2	Counter-propagating fields in a Fabry-Perot cavity	4
1.3	Sketch of a vertical-cavity surface-emitting semiconductor laser. The actual configuration represents a top-emitting oxide-confined VCSEL	6
1.4	Materials for VCSELs in a wide spectral band	7
2.1	Band structure of a strained quantum well conceptually replaced by a four-level system in the spin flip model	13
2.2	Polarization of the field vector in the VCSEL cavity	14
2.3	Linear stability of the linearly polarized solutions	21
2.4	Polarization of the field vector in the VCSEL cavity	22
3.1	Intensity noise and cross correlation of the $5\mu\text{m}$ device measured through a Glan-Thompson polarizer	24
3.2	Regions of operation represented in the phase diagram current vs. spin flip.	27
3.3	Evolution of the effective birefringence as function of the injection current in the limit of small linear anisotropies	28
3.4	Effective birefringence and effective dichroism as function of the injection current for three different spin flip rates	30
3.5	Schematic representation of the optical spectra of the lasing and non-lasing components of the electric field	31
3.6	Power spectra in arbitrary units for currents below PS and above PS	35
3.7	Temporal trace of the intensity components and their respective probability density function	36
3.8	Poincaré sphere: $x(y)$ -LP state along the $\hat{x}(\hat{y})$ direction; c^\pm are right and left circularly polarized states, ε^\pm are right and left ellipti- cally polarized states. Shaded circles represent fluctuations around these states	38
3.9	Power spectra (in arbitrary units) of the polarization fluctuations within a COs region and when crossing a polarization switching . .	40

3.10	Power spectra (in arbitrary units) of the polarization fluctuations in the limit of weak linear anisotropies.	40
3.11	Study of the effect of γ_s in the absence of birefringence, in the power spectra of the circular and linear components. Evolution of the polarization state on the Poincaré sphere for small and moderate values of the spin flip rate	42
3.12	Study of the effect of γ_p on power spectra of the circular and linear components when for moderate values of γ_s . Evolution on the Poincaré sphere for small and moderate birefringence	43
3.13	Normalized crosscorrelation of the circular components C_{+-} and the linear components C_{xy}	45

Resum

Els nombrosos avanços realitzats en el camp dels làsers i de l'electrònica quàntica durant les darreres dècades ha potenciat la implantació d'aquests dispositius en moltes aplicacions que han passat a formar part de la vida quotidiana. Cal anomenar d'entre elles, els sistemes de comunicacions òptiques, la gigant expansió d'Internet, lectors de disc compactes, punters làser, impresores làser; sense deixar de banda les aplicacions mèdiques i industrials. El desenvolupament dels làsers de semiconductor i la recerca de tècniques per al seu perfeccionament han fet d'aquests uns dispositius òptims per la utilització, especialment en sistemes de comunicacions òptiques. El disseny d'estructures amb noves geometries i basades en nous materials ha donat com a fruit làsers de semiconductor amb unes característiques de funcionament peculiars. Els làsers de cavitat vertical i emissió per superfície, també coneguts com VCSELs, han atret l'atenció de molts de grups científics, anant desde el punt de vista més aplicat fins el de la física fonamental. Es sabut que els VCSELs són millors que els làsers de semiconductor convencionals o d'emissió lateral en diversos aspectes, encara que poden presentar inestabilitats associades amb la polarització i l'excitació d'estructures espacials d'ordre superior. Algunes aplicacions necessiten que la polarització i la forma transversal del camp elèctric en aquests aparells sigui estable i ben controlada. Aquest fet motiva l'estudi, caracterització i control de la polarització i de la dinàmica transversal. En aquest treball s'aprofundeix en l'estudi de les propietats de polarització en VCSELs. En particular, s'estudia la repercussió de les fluctuacions de les components de polarització sobre les característiques de l'emissió làser. Aquestes fluctuacions provenen de processos quàntics d'emissió espontània de fotons que s'acoblen al mode òptic d'emissió. Les característiques de les fluctuacions de la llum emesa reflecteixen de manera natural els mecanismes físics involucrats, proporcionat una possible interpretació dels resultats experimentals quan són comparats amb la teoria.

La memòria està organitzada en quatre capítols. En el tema 1, es recullen de manera esquemàtica alguns conceptes essencials de la física del làser. Aquests es van introduint de manera successiva presentant-los dins d'un contexte històric. Amb aquestes eines, és possible presentar les característiques bàsiques de funcionament dels VCSELs al final del capítol. En el tema 2, s'aprofundeix en qüestions de modelat, posant especial interès en les fonts de renou, les propietats de polarització i els processos de relaxació d'espí.

S'introdueix el *spin flip model* (SFM), que en presència de renou d'emissió espontània, representa un marc teòric per descriure la dinàmica de polarització en VCSELs. Al final del tema, presentam el model SFM lineariatzat, que constitueix el punt de partida per l'estudi de les fluctuacions de polarització. En el tema 3, part fonamental d'aquest treball, es discuteix, desde un nivell semiclàssic, les fluctuacions de les components de polarització de la llum emesa. Per tal d'entendre el comportament de les fluctuacions, es necessari primer introduir alguns conceptes que provenen de l'anàlisi lineal de les equacions SFM. Conceptes com anisotropies no-lineals, birefringència efectiva, i règims d'operació són seqüencialment introduïts. També es discuteixen els espectres de potència, que mostren la magnitud de les fluctuacions a diferents freqüències, de les components lineals i circulars del camp elèctric. L'estudi es completa donant a conèixer l'evolució del l'estat de polarització utilitzant la representació de l'esfera de Poincaré. Aquesta esfera és una projecció de la dinàmica sobre un sistema de coordenades esfèriques descrites per dos angles de polarització. Els espectres de potència dels angles de polarització són descrits en les diverses regions d'operació. També es mostra la importància d'alguns paràmetres rellevants sobre la dinàmica de polarització i les seves fluctuacions. Al final del capítol es descriu la correlació, experimentalment observades, que existeix entre les distintes components de polarització. Finalment, en el tema 4 presentam les conclusions del treball i algunes perspectives relacionades amb qüestions de modelatge.

Palma, Octubre de 2001

Josep Mulet Pol

Outline

The important advances in the laser field and quantum electronics, carried out in the last decades, have led to a variety of everyday life applications for these devices. Some examples include: optical communication systems, the explosive growth of Internet applications, CD players, laser pointers, laser printers, as well as medical and industrial applications. The development of semiconductor lasers and the techniques to improve their performance have provided devices very attractive for applications, specially in optical communication systems. The design of new structures as well as the implementation of novel materials have led to semiconductor lasers with rather peculiar performance. Vertical-cavity surface-emitting lasers, hereafter VCSELs, have sparked the interest of many scientific groups, covering from the most applied point of view to that of the fundamental physics. It is well known that VCSELs present a number of advantages with respect to the conventional edge-emitting semiconductor lasers, although they may display instabilities associated with the polarization and transverse degrees of freedom. In many applications, it is crucial to achieve devices emitting in a well stabilized and controlled polarization and transverse mode. This fact motivates the study, characterization and control of polarization and transverse dynamics in VCSELs. In this work, we investigate the impact of polarization components fluctuation in the characteristics of the laser emission. These fluctuations arise from spontaneous emission processes governed by the laws of quantum mechanics. The features of these fluctuations can be regarded as fingerprints of the involved physical mechanisms, thus providing a natural interpretation of the experimental results when comparing with theory.

This report is organized in four chapters as follows. In chapter 1, we sketch some fundamental concepts required to introduce the laser physics. We introduced them sequentially within an historical perspective. With the help of these concepts, it is then possible to outline the working principles of VCSELs. In chapter 2, we focus on modeling issues, and particularly, on the spontaneous emission noise sources, polarization properties, and spin relaxation processes. We introduce the *spin flip model* (SFM) that provides a theoretical framework to describe the polarization dynamics in VCSELs. At the end of chapter 2, we introduce the linearized SFM, being the starting point to study polarization fluctuations. In chapter 3, the main part of this work, we discuss within a semiclassical framework, the fluctuations of the polarization components. In order to understand the behavior of fluctuations, it is first necessary to introduce some concepts that arise from the linear stability analysis of the SFM. Concepts like non-linear anisotropies, effective birefringence, and regimes of operation are sequentially introduced. Thereafter, we analyze the power spectra, that reflect the magnitude of fluctuations at different frequencies, of the linear and circular components of the electric field. A complete understanding of the polarization dynamics is possible by intro-

ducing the Poincaré sphere representation. The later is a projection of the dynamics onto a spherical coordinate system described by two polarization angles. The power spectra of the polarization angles fluctuations are also shown in several regions of operation. We also give evidences of the role of some relevant parameters that affect the polarization dynamics and its fluctuations. At the end of chapter 3, we describe the correlation, that has been experimentally observed, among different polarization components. Finally in chapter 4, we present the conclusions as well as some perspectives related to modeling issues.

Palma, October 2001

Josep Mulet Pol

Chapter 1

Introduction

1.1 A brief history about lasers

THE origins of the laser¹ can be traced back to the Einstein's concept of stimulated emission, derived in 1917 from Planck's law of radiation. The presence of a photon, with appropriate frequency, can stimulate an excited atom to emit a photon with identical phase, frequency and propagation direction that the incident one. From this mechanism results the properties of the laser light: large monochromaticity, optical coherence, directionality, and brightness. It is surprising however that most of the light emitted by common sources –bulbs, the sun, LEDs– arises from spontaneous emission. In order to increase the probability of having stimulated emission in front of spontaneous emission, it is important to achieve highly populated excited states with long lifetimes (population inversion). From Boltzmann's law, the population of an energetic level, under thermodynamic equilibrium, decreases when increasing the energy of such state. Therefore, population inversion must be achieved by providing energy to the system from an external source (pumping). The pump mechanism varies depending on the type of laser, being: electric discharge in gas lasers, a flash lamp in solid state lasers, and current injection in semiconductor (sc) lasers, etc. The light amplification understood as an avalanche of identical photons can be generated by inserting the system in to a cavity that feeds back the optical field (resonator). Therefore, three ingredients are fundamental in any laser: a pump that generates population inversion, a medium providing gain/amplification, and a cavity confining the optical field. The first population inversion was attained in ammonia molecules passing through an electrostatic focuser by Townes and Shawlow [1] in 1954. The constructed device, originally called MASER, emitted light in the microwave range. The first successfully optical laser in the visible spectrum was constructed by Maiman [2], and consisted of a ruby crystal surrounded by a helicoidal flash tube. This advent was followed, at the ends of the same year, by the experimental demonstration of working He-Ne gas lasers.

¹LASER is the acronym of Light Amplification by Stimulated Emission of Radiation.

1917	<i>A. Einstein</i> : postulate of stimulated emission of photons
1954	<i>C. H. Townes and A. L. Schalow</i> : the first NH_3 MASER
1960	<i>T. H. Maiman</i> : demonstrates the first optical ruby laser
1962	Experimental demonstration of the first sc laser
1965	<i>Melngailis</i> : the first bulk InSb SE laser
1977	<i>K. Iga</i> : heterostructure SE laser
1979	<i>H. Soda</i> : first VCSEL pulsed lasing at 77K, with $I_{th} = 900\text{mA}$
1984	<i>K. Iga</i> : pulsed GaAlAs/GaAs VCSEL at room temperature
1985	<i>A. Chailertvanitkul</i> : introduces sc multilayer reflectors
1988	CW operation of VCSELs at room temperature
1989	<i>J. L. Jewell</i> : QW and multilayer reflector, low threshold 1-2 mA
1996	First commercial applications of VCSELs
1997	<i>D. G. Deppe</i> : introduces Quantum-Dot VCSELs
2000	New materials for development of blue-UV VCSELs

Table 1.1: Chronology of some significant advances in lasers and VCSELs.

However, semiconductors were too different to an “atomic” system, and too poorly understood, to profit much from the success with ruby and gas lasers. It was not until the mid-50s that experimental evidence emerged of the existence of both direct and indirect band-gap semiconductors, a difference decisive in determining whether a material will be an efficient light emitter or not. The feasibility of stimulated emission in semiconductors was considered by the early 60’s but there was no motivation to explore the possibilities as it was believed that the emission would be weak. However in 1962 a group from MIT Lincoln Labs reported emission of radiation, using Zn-diffused GaAs p-n junction, and transmission of the light over a considerable distance. This report sparked great interest and before the year was out, four groups reported working semiconductor lasers [3].

1.2 Semiconductor lasers

Semiconductor lasers are based on forward biased p-n junctions of sc materials –diode lasers–. The concept of a carrier in a sc laser is associated with an electron in the conduction band and a hole in the valence band providing an electron-hole pair. The recombination of an electron-hole pair, that is more efficient in direct band-gap sc, provides the emission of a photon. Pop-

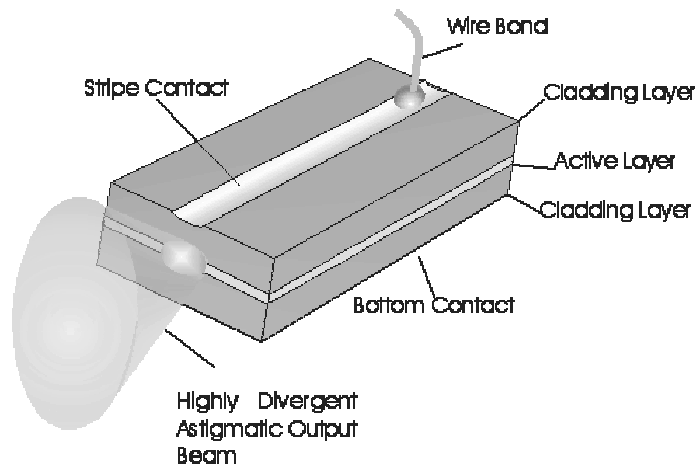


Figure 1.1: Sketch of an edge-emitting semiconductor laser.

ulation inversion is obtained by localizing in a spatial zone, known as active region, a large number of electron-hole pairs. This can be achieved using an heterostructure, i.e., by inserting the active region between two sc materials of wider band-gap. In turn, this heterostructure provides lateral confinement of the electric field due to the higher refractive index in the central region. The most important class of semiconductor diode lasers are based on III-V compounds, for instance GaAlAs/GaAs². The optical gain is accomplished by injecting minority carriers into the thin active layer. However, optical gain alone is not enough to operate a laser. The polished facets perpendicular to the junction plane provides the optical feedback by forming a Fabry-Perot cavity, which role is twofold. First, it selects a preferred direction for stimulated emission and second, it introduces a frequency selective mechanism that leads to the longitudinal cavity modes. The injected current has to exceed a certain threshold current, situation in which the optical gain equals the losses, in order to start the laser operation.

Depending on the geometry and dimensions of the cavity, lasers are classified in edge-emitting lasers (EELs) and vertical-cavity surface-emitting lasers (VCSELs). In an EEL, sketched in Fig. 1.1, the light propagates in a rectangular waveguide which longitudinal extent coincides with the active layer. Their mirrors are formed by cleaving a wafer along the crystal planes to form smooth facets. If necessary, dielectric materials are subsequently deposited to reach the desired reflectivity. No external mirrors are in general required, since cleaved facets of sc already provide sufficient reflectivity to allow laser operation. On the contrary, mirrors with very high reflectivity are required in VCSELs as we will show later.

²The notation $\text{Ga}_{1-x}\text{Al}_x\text{As}/\text{GaAs}$, with x the molar fraction of Al, represents the nature of the materials forming the heterostructure, i.e. a “sandwich” of GaAlAs/GaAs/GaAlAs.

Longitudinal modes

Let us consider a passive medium, which does not provide any amplification, with refractive index n_e filling the space between two partially reflecting mirrors, with internal power reflectivities $R_{1,2}$, and separated by a distance L [Fig. 1.2]. The optical field in the resulting Fabry-Perot cavity can be expressed as

$$\mathcal{E}(z; \omega) = E_{\omega}^{+} e^{iq_{\omega}z} + E_{\omega}^{-} e^{-iq_{\omega}z},$$

where E_{ω}^{\pm} are the amplitudes of two counter-propagating plane waves. The complex longitudinal propagation constant q_{ω} is determined from boundary conditions at the two mirrors providing the roundtrip condition

$$[R_1(\omega)R_2(\omega)]^{1/2} e^{-2\text{Im} q_{\omega}L} e^{i(\Phi_1(\omega)+\Phi_2(\omega)+2\text{Re} q_{\omega}L)} = 1, \quad (1.1)$$

where $\Phi_1(\omega), \Phi_2(\omega)$ stand for the frequency dependent (internal) phase reflectivities of the mirrors. Standing waves in the cavity are only possible for a discrete number of frequencies that define the longitudinal cavity modes. The frequency mode spacing reads [4]

$$\Delta\nu = \frac{c}{2n_g L}, \quad (1.2)$$

$n_g \equiv \frac{d}{d\omega}(\omega n_e)$ being the group refractive index and c the speed of the light in vacuum. Typical values for EELs are $n_e = 3.5$, $n_g = 4.0$, and $L = 250 \mu\text{m}$ which provides $\Delta\nu \approx 150 \text{ GHz}$. A larger mode spacing is obtained in microcavities where $L \approx 1 \mu\text{m}$, and thus $\Delta\nu \approx 40 \text{ THz}$. The gain curve of the active material has a bandwidth of $\sim 2 \text{ THz}$, hence, in typical EELs, up to 20 longitudinal modes can profit of the material gain. On the contrary, only one longitudinal mode can be amplified in VCSELs. It is well known that multimode emission affects the performance of the device in data-transmission applications because of an enhanced pulse dispersion during fiber propagation. For this reason, VCSELs are attractive devices due to their single-longitudinal mode emission. A drawback is that high-order transverse modes, that extend across the lateral directions, are more easily excited in VCSELs due to their higher Fresnel number $N = d^2/(\lambda L)$, d being the typical lateral length scale and λ the emission wavelength. In addition, the short cavity of the VCSEL strongly affects the losses through the mirrors.

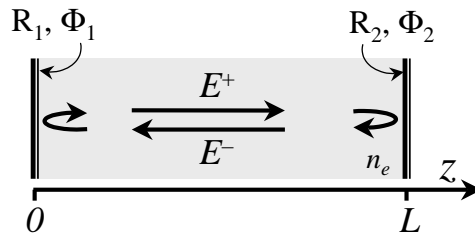


Figure 1.2: Counter-propagating fields in a Fabry-Perot cavity.

Since the mirrors are partially reflecting, a fraction of photons escape through the mirrors leading to a decay of the electric field within the cavity. Moreover, the electric field is absorbed in the different material layers constituting the laser. Thus, the amplitude of the electric field decays at a rate

$$\kappa = \frac{c}{2n_g} \left[\alpha_{int} + \frac{1}{2L} \ln \left(\frac{1}{R_1 R_2} \right) \right], \quad (1.3)$$

where α_{int} represents the internal losses. Typical power reflectivities, in EELs, of $R_1 = R_2 \approx 0.3$ and $\alpha_{int} = 16 \text{ cm}^{-1}$ leads to $\kappa \approx 300 \text{ ns}^{-1}$. Since in a microcavity L is much smaller, the reflectivity of the mirrors have to be enhanced in order to maintain the same cavity decay rate κ .

1.3 Surface-emitting semiconductor lasers

A VCSEL is a particular type of semiconductor laser in which the resonating cavity is perpendicular to a thin active layer. In contrast to conventional EELs, the optical beam is guided and emitted in the vertical direction [See Fig. 1.3(b)]. The thin active layer ($\sim 10 - 30 \text{ nm}$) is composed by one or several quantum wells³ providing high optical gain, low threshold current, high relaxation oscillation frequency, and improved temperature characteristics. It is worth noting that the single gain-path length in a VCSEL is extremely small, typically of 1% of the cavity length, i.e. four orders of magnitude shorter than an EEL. Thus, to make a VCSEL, it is imperative to fabricate mirrors with very high reflectivities, an active region with high optical gain, and a cavity with very low optical losses. The VCSEL's mirrors are created by growing a stack of quarter-wavelength layers of sc materials with alternating refractive indexes, forming a distributed Bragg reflector (DBR). The order of 20-40 pairs are necessary to achieve high reflectivities ($> 99.6\%$). The electric current is injected in a disc or ring-shaped contact in bottom-emitter and top-emitter devices, respectively. Carrier transport along the different layers determines the lateral distribution of current density in the active layer, that in turn delimits the lateral extension of the active region. The current is localized close to the cavity axis by proton implantation in gain-guided devices while oxide-layers are used in oxide-confined VCSELs. In the former, the lateral confinement of the optical mode occurs through a combination of gain-guiding and carrier antiguiding mechanisms [5], while in the later the oxide layer, with lower refractive index, provides an index-step waveguide that confines the electric field.

The typical dimensions, length \times width \times thickness, in an EEL differs considerably with respect to a VCSEL, being in the first $250 \times 300 \times 10 \mu\text{m}^3$ while in

³A thin layer of GaAs bounded on either side by GaAlAs, confine electrons and holes. If the thickness of the GaAs layer is smaller than $\sim 200 \text{ \AA}$, the confinement energies become quantified and the heterostructure is known as quantum well laser.

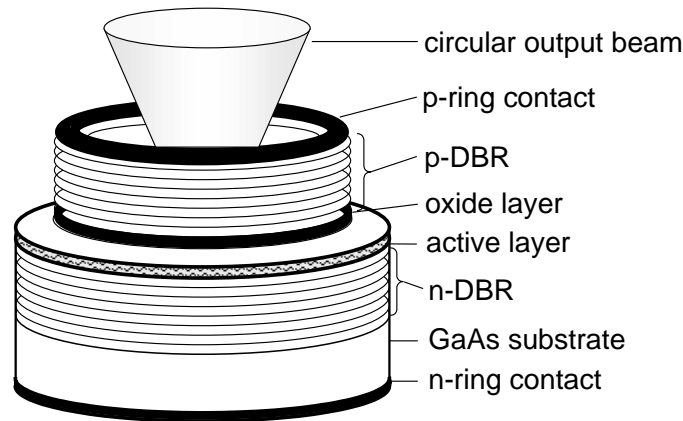


Figure 1.3: Sketch of a vertical-cavity surface-emitting semiconductor laser. The actual configuration represents a top-emitting oxide-confined VCSEL.

the second $1 \times 10 \times 10 \mu\text{m}^3$. An important consequence is that VCSELs emit in a single-longitudinal mode. In addition, the geometry of the VCSEL's cavity is circular, in contrast to EELs with a rectangular shape. As a consequence, the polarization of the electric field in an EEL is determined by the structure, being transverse electric (TE) or transverse magnetic (TM) depending whether the electric or the magnetic field is linearly polarized along the heterojunction plane. However, polarization in VCSELs is not so well stabilized due to their circularly symmetric cavity. This fact motivates the understanding, characterization and control of polarization in VCSELs. Since in many practical situations the polarization degrees of freedom in EELs are disregarded, the description of polarization effects in VCSELs requires of a thorough revision of the involved microscopic processes. The next chapter is devoted to introduce a model that accounts for the fundamental physical mechanisms governing the polarization dynamics in quantum well VCSELs.

From an illusion to a reality

Certainly, VCSELs that are currently commercially available, have been the fruit of the continuous development of the semiconductor technology and growth techniques. The first surface emitting (SE) laser was experimentally demonstrated by Melngailis already in 1965. The active material consisted in a piece of bulk InSb, refrigerated at 10K and immersed in an intense magnetic field in order to confine the carriers. The concept of heterostructure in SE laser was introduced by K. Iga (1977) as an alternative method to improve the carrier confinement. Exploiting this idea, H. Soda in 1979 obtained pulsed operation of GaInAsP/InP SE with threshold current of 900mA operating at 70K. The threshold current of these initial SE devices was so high because the reflectivity of the metallic mirrors was insufficient. In 1984, K. Iga replaced them by semiconductor mirrors obtaining pulsed operation of

GaAlAs/GaAs VCSEL at room temperature. Important improvements were achieved after the introduction of multilayer mirrors and also when replacing the bulk active material by quantum wells. With this new technology, Jewell et al. (1989) grew VCSELs with threshold currents as low as 1-2mA operating continuous wave (CW) at room temperature. The first commercial applications of VCSELs started to appear since 1996, being suitable for local area networks (LANs), optical interconnects, and for future applications in the gigabit Ethernet as well. By a proper combination of materials it is possible to construct devices emitting at different wavelengths [See Fig. 1.4]. The importance of GaInAsP/InP VCSELs operating at 1.3 or 1.55 μm is increasing, since their potential application in parallel lightwave systems and parallel optical interconnects. Some commercial links are also available with AlGaAs/GaAs VCSELs emitting near 0.85 μm . Red emitting VCSELs, based on GaAlInP/GaAs materials, are also attractive for their applications in CD players and plastic optical fiber systems. Green-blue and blue VCSELs are, in general, more difficult to obtain displaying high threshold currents, short lifetimes and in many cases only pulsed operation. The applications of blue VCSELs is huge, for instance, in full color displays, and high efficiency illumination together with green and red devices.

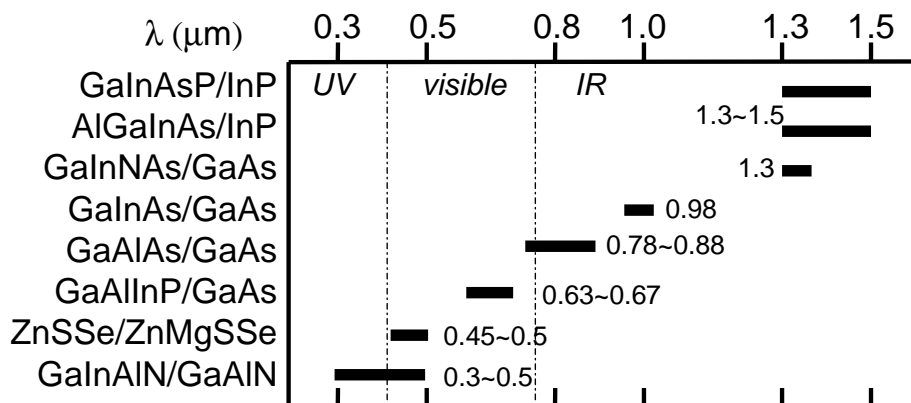


Figure 1.4: Materials for VCSELs in a wide spectral band. Extracted from Ref. [6].

Chapter 2

Fundamentals of the VCSEL Modeling

2.1 Quantum Noise

SINCE the development of a modern semiconductor technology, it has been possible to construct semiconductor structures in the nanometer scales and reducing the laser size up to a single wavelength limit. Due to this constant reduction of scales, quantum effects in the confinement of electrons and in the light field have increased considerably. As consequence, the laser light field is organized in random quantum fluctuations arising from spontaneous emission processes. A correct treatment requires of quantization of the electric fields and dipole amplitudes [7]. We instead consider that, in a sufficiently intense field, the deterministic field dynamics is well described by the classical Maxwell's equations [7, 8]. In any case, the sc material dynamics has to be treated by using quantum mechanics. Within this semiclassical approach, the quantum fluctuations are modeled by means classical Langevin noise sources. Obviously, the strength of these fluctuations can only be determined from quantum mechanical requirements.

This section is devoted to introduce some fundamental concepts of Langevin equations, in which the chapter 3 is mainly based. Thereafter, the equations describing the polarization dynamics of VCSELs in presence of quantum noise are considered.

Semiclassical Langevin equations

As an starting point, we consider that a complex dipole's amplitude σ , in absence of electric field and decaying at rate γ_{\perp} , is governed by the simple Langevin equation

$$\frac{d\sigma}{dt} = -\gamma_{\perp}\sigma + f(t), \quad (2.1)$$

where $f(t)$ is a rapidly fluctuating random term. A mathematical formulation of such a highly irregular function, is that $f(t)$ and $f(t')$ are statistically independent when $t \neq t'$. Hence, the correlation function $\langle f(t)f^*(t+\tau) \rangle = 2\mathcal{D}\delta(\tau)$, \mathcal{D} being the diffusion coefficient, is zero everywhere except at $\tau = 0$ where has the rather pathological result of an infinite variance. Furthermore, we also require that $f(t)$ has zero mean, i.e. $\langle f(t) \rangle = 0$, where $\langle \dots \rangle$ means average over different noise realizations. An object with these properties is known as complex white Gaussian noise.

The formal solution of Eq. (2.1) can be expressed as

$$\sigma(t) = \sigma(0)e^{-\gamma_{\perp}t} + \int_0^t dt' f(t')e^{-\gamma_{\perp}(t-t')}. \quad (2.2)$$

If one assumes that the initial condition is deterministic or Gaussian distributed, then mean value and variance of $\sigma(t)$ read

$$\langle \sigma(t) \rangle = \langle \sigma(0) \rangle e^{-\gamma_{\perp}t}, \quad (2.3a)$$

$$\begin{aligned} \text{var}\{\sigma(t)\} &= \langle \sigma(t)\sigma^*(t) \rangle - |\langle \sigma(t) \rangle|^2 = \\ &= \left(\text{var}\{\sigma(0)\} - \frac{\mathcal{D}}{\gamma_{\perp}} \right) e^{-2\gamma_{\perp}t} + \frac{\mathcal{D}}{\gamma_{\perp}}. \end{aligned} \quad (2.3b)$$

Making use of these results, the correlation function of $\sigma(t)$ can be expressed as follows

$$\langle \sigma(t)\sigma^*(t+\tau) \rangle = [|\langle \sigma(t) \rangle|^2 + \text{var}\{\sigma(t)\}] e^{-\gamma_{\perp}|\tau|}. \quad (2.4)$$

In the case of a stationary process σ_s , being that in which statistical properties are time independent, we have

$$\langle \sigma_s(t)\sigma_s^*(t+\tau) \rangle = \lim_{t \rightarrow \infty} \langle \sigma(t)\sigma^*(t+\tau) \rangle = \frac{\mathcal{D}}{\gamma_{\perp}} e^{-\gamma_{\perp}|\tau|}, \quad (2.5)$$

which describes an Ornstein-Uhlenbeck process that displays a more realistic correlation function when comparing with a white noise $f(t)$. Note however that the σ_s process tends to a white noise in the limit of large damping

$$\gamma_{\perp}^2 \langle \sigma_s(t)\sigma_s^*(t+\tau) \rangle \xrightarrow{\gamma_{\perp} \rightarrow \infty} 2\mathcal{D} \delta(\tau). \quad (2.6)$$

The consistent semiclassical description of quantum noise must be formulated in such a way that the noise terms acting on the fields and dipoles always preserve the uncertainty relations of the corresponding quantum operators. Let's assume that at $t = 0$, $\text{var}\{\sigma(0)\} = \frac{1}{2}$. From Eq. (2.5), the variance of $\sigma_s(t)$ reads

$$\text{var}\{\sigma_s(t)\} = \frac{\mathcal{D}}{\gamma_{\perp}}. \quad (2.7)$$

Hence, we assure that $\text{var}\{\sigma(t)\} = \frac{1}{2}$ only when $\mathcal{D} = \gamma_{\perp}/2$. In dissipative systems, the loss of quantum noise must be compensated by a corresponding fluctuation of the time derivative. This rough justification can be rigorously presented in terms of the quantum mechanical fluctuation-dissipation theorem [9, 10], that determines

$$\langle f(t)f^*(t+\tau) \rangle = \gamma_{\perp}\delta(\tau). \quad (2.8)$$

In the case of an ensemble of N_0 dipoles providing a macroscopic material polarization $P = \sum_i \sigma_i$, Eq. (2.8) is generalized to $\langle F(t)F^*(t+\tau) \rangle = \gamma_{\perp}N_0\delta(\tau)$.

In many calculations, it is useful to define the Fourier transform of a white Gaussian noise $f(t)$ as

$$\tilde{f}(\omega) = \int_{-\infty}^{\infty} dt f(t)e^{-i\omega t}. \quad (2.9)$$

The Fourier transformed white Gaussian noise $\tilde{f}(\omega)$ has a correlation

$$\langle \tilde{f}(\omega)\tilde{f}^*(\omega') \rangle = 2\mathcal{D}\delta(\omega - \omega'). \quad (2.10)$$

A more convenient way to describe a generic stationary noise process $G_s(t)$ is by means of the spectral density function at frequency ω [11]

$$S_G(\omega) \equiv \int_{-\infty}^{\infty} \langle \tilde{G}_s(\omega)\tilde{G}_s^*(\omega') \rangle d\omega' = \int_{-\infty}^{\infty} \langle G_s(t)G_s^*(t+\tau) \rangle e^{-i\omega\tau} d\tau, \quad (2.11)$$

a result of the Wiener-Khintchine theorem. In the case of a white noise, $G_s(t) = f(t)$, the spectral density function reduces to $S_f(\omega) = 2\mathcal{D}$, which implies that Langevin noise sources have a white (frequency-independent) spectrum. Finally for the Ornstein-Uhlenbeck process σ_s

$$S_{\sigma}(\omega) = \frac{2\mathcal{D}}{\omega^2 + \gamma_{\perp}^2}, \quad (2.12)$$

which display a Lorentzian lineshape function. The generalization of Eqs. (2.11) and (2.12) to a linear system of n differential equations is given in Ref. [11]. A review of stochastic processes and its application to physical systems can be found in Ref. [12]. Finally, the Itô transformation from the complex field amplitudes to power and phase representation is described in Appendix B.

Spontaneous emission factor and rate

There exists a variety of definitions to give account of the amount of quantum noise. In this section we summarize some important quantities related to noise measurements.

The spontaneous carrier lifetime τ_{sp} , defined as the time required for a carrier in a two level atom to decay to the ground state is [10]

$$\tau_{sp}^{-1} \equiv \gamma = \frac{1}{\hbar\omega_0} \frac{1}{4\pi\epsilon} \frac{4\omega_0^4}{3c^3} \mathbf{d}_{cv}^2, \quad (2.13)$$

where $\hbar\omega_0$ is the transition energy, $\epsilon = \epsilon_0\epsilon_r$ the dielectric constant of the medium and \mathbf{d}_{cv} is the dipole's matrix element.

The spontaneous emission rate, at resonance, can be expressed as β_0/τ_{sp} where $\beta_0 < 1$ is the fraction of spontaneously emitted photons that go into the lasing mode. In addition, $\beta_0 N/\tau_{sp}$ represents the number of spontaneous emission events during a second that couples with the lasing mode, N representing the degree of inversion. The spontaneous emission factor in a QW is given by

$$\frac{\beta_0}{\tau_{sp}} = \frac{g_0^2}{\gamma_{\perp}} \left(\frac{v_0}{\sigma^{-1}A_{\perp}} \right) \equiv \frac{g_{QW}^2}{\gamma_{\perp}}, \quad (2.14)$$

v_0 being the volume of the elementary lattice cell, $\sigma^{-1}A_{\perp}$ a geometrical correction that stands for the volume of the optical mode within the QW layer, and g_0 the dipole-field interaction rate

$$g_0 = \sqrt{\frac{\omega_0}{2\hbar\epsilon v_0}} |\mathbf{d}_{cv}|.$$

Since only a small fraction of the spontaneous emission processes successfully couples with the field mode, we can define an effective dipole-field interaction rate in QWs, at resonance, g_{QW} in analogy to Eq. (2.14)

$$g_{QW}^2 = \gamma_{\perp} \gamma \beta_0. \quad (2.15)$$

Typical values for these parameters at $\hbar\omega_0 \approx 1.5\text{eV}$ are $\tau_{sp} = \gamma^{-1} = 10^{-9}\text{s}$, $\gamma_{\perp} = 10^{13}\text{s}^{-1}$, $g_0 = 2 \times 10^{15}\text{s}^{-1}$, $v_0 = 4 \times 10^{-29}\text{m}^3$, $\sigma^{-1}A_{\perp} \approx 10^{-14}\text{m}^3$. Hence, the resulting spontaneous emission factor is $\beta_0 = 10^{-6}$, and the coupling rate $g_{QW} = 10^8\text{s}^{-1}$. With this choice of parameters, we get a correct order of magnitude of 10^{12}s^{-1} in the product $\beta_0 N/\tau_{sp}$.

2.2 Polarization Dynamics

The light emitted by an EEL is usually transverse electric (TE) or magnetic (TM) linearly-polarized along the heterojunction plane of a rectangular-shaped resonator. However, the polarization in VCELs is not so well stabilized due to their inherent circular geometry. For this reason, it is known that VCSELs display a number of polarization instabilities, such as polarization switching when the injection current is increased and excitation of

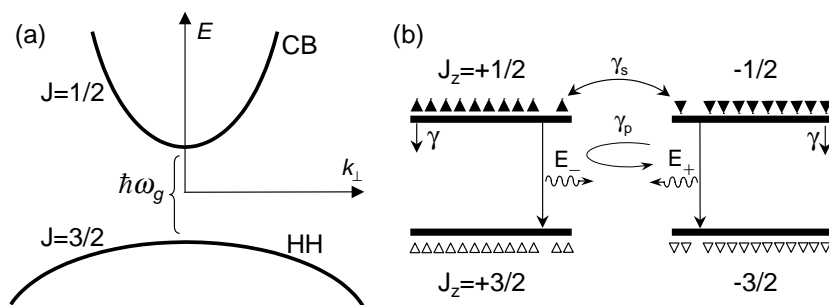


Figure 2.1: Band structure of a strained quantum well (a) conceptually replaced by a four-level system in the spin flip model (b). Allowed transitions, recombination and mixing mechanisms are indicated in this figure.

transverse modes as well. These aspects motivate the investigation of the underlying mechanisms governing the polarization mode selection in VCSELs. Polarization fluctuations reflect themselves in the properties of the polarization dynamics. Consequently, a thorough understanding of the polarization fluctuations induced by quantum noise should provide a valuable theoretical prediction to be contrasted with experimental results.

The polarization of laser light is of quantum nature and it originates in the spin sublevels of the lasing transitions between the conduction and valence bands of the semiconductor material. In a surface-emitting laser the light propagates along the quantization axis of the QW. Hence selection rules for the optical transitions are restricted to changes in the total angular momentum of $\Delta J_z = \pm 1$, corresponding to the emission of a right and left circularly polarized photon, respectively. The band structure of a QW can be ideally replaced by a plenty of coupled two level systems labeled by its transverse electron wavevector k_{\perp} . A considerable simplification consists in analyze the band structure of direct band-gap strained QW around $k_{\perp} = 0$. The original spin flip model (SFM) [13] considers the optical transitions in this four level system [See Fig. 2.1]. The SFM is based on a generalization of the gas laser theory to the magnetic sublevels of the conduction and heavy-hole bands of a QW. The conduction band is replaced by two levels populated by electrons with opposite spin orientations and angular momenta $J_z = \pm 1/2$. In the same way, the heavy hole band (HH) is replaced by two levels populated by holes with opposite spin orientations and $J_z = \pm 3/2$. As already commented, due to the quantum-mechanical selection rules, the interaction with the active material is diagonal in the basis of circularly polarized states. It is then natural to split the total carrier density into spin-up and spin-down carrier reservoirs. The population inversion in the two spin channels is given by $N_{\pm} \equiv N_{\pm}^c - N_{\pm}^v$, where N_{\pm}^c stand for the population in the conduction spin subbands while N_{\pm}^v in the valence spin subbands. The split-off band, with higher energy than the heavy-hole band, does not become optically active until quite high inversion densities, thus in first approximation it can be disregarded. In addition, it is

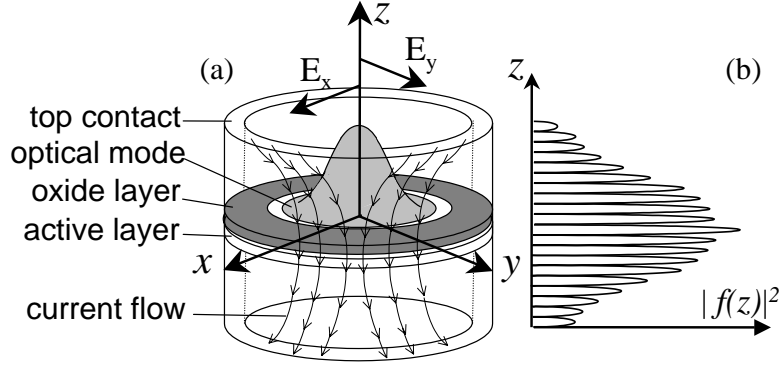


Figure 2.2: (a) Polarization of the field vector in the VCSEL cavity. Arrows represent the carrier transport from the top to the bottom electrical contacts. The oxide layer determines the active region and the shape of the optical mode which is assumed Gaussian. (b) Standing wave in the longitudinal direction.

assumed that the two spin channels are energetically degenerated.

The evolution of the electric field within the VCSEL cavity is governed by the well known Maxwell's equations [8], that lead to the wave equation in Fourier domain

$$\left\{ \nabla^2 + \frac{\omega^2}{c^2} [n_e^2(\vec{r}; \omega) + i\alpha_i(\vec{r}; \omega)] \right\} \vec{\mathcal{E}}(\vec{r}; \omega) = -\frac{\omega^2}{c^2} \frac{\vec{\mathcal{P}}(\vec{r}; \omega)}{\varepsilon_0} R_W(z_0), \quad (2.16)$$

$\nabla^2 = \partial_x^2 + \partial_y^2 + \partial_z^2$ and $c^2 = 1/(\varepsilon_0\mu_0)$. $n_e(\vec{r}; \omega)$ stands for the refractive index of the passive medium filling the cavity, while $\alpha_i(\vec{r}; \omega)$ represents the absorption. $\vec{\mathcal{P}}(\vec{r}; \omega)$ is the active region contribution to the material polarization being non-vanishing only in the QW layer(s). The rectangle function $R_W(z_0)$ delimits the position of the quantum well(s). We also assume¹ that the field is totally polarized in the plane transverse to the cavity axis and propagating along the longitudinal direction [Fig. 2.2]

$$\vec{\mathcal{E}}(\vec{r}; t) = f(z) [A_x(\vec{r}_\perp; t)\hat{x} + A_y(\vec{r}_\perp; t)\hat{y}] e^{i\Omega t}. \quad (2.17)$$

$f(z)$ describes the standing wave of the electric field between the top and bottom Bragg mirrors. Since DBR mirrors are nearly perfect reflectors, $f_n(z) \approx \sin(q_n z)$ with $q_n = n\pi/L$, L being the physical separation between the two mirrors. The QW layer has to be placed close to an anti-node of $f(z)$ in order to maximize the overlapping with the electric field. $\Omega = cq_n/n_e$ is the longitudinal cavity-mode resonant frequency. $A_{x,y}$ stand for the slowly-varying (with respect to Ω) linearly-polarized components of the electric field². Although the cavity is circularly symmetric, the constituent materials have a

¹This hypothesis is justified in gain-guided and in weakly index-guided VCSELs, and being the exact solution of Maxwell's equations in the limit of weak lateral guidance.

²Note that we have used the following criteria to define the Fourier transform, $A(\omega) = \int_{-\infty}^{\infty} dt A(t) e^{-i\omega t}$

cubic symmetry. Thus, the unitary cartesian vectors \hat{x}, \hat{y} usually correspond to the underlying crystallographic axes. It has been already commented that the circular basis is the natural representation for the lasing transitions in QWs. The electric field expressed in the circular basis reads

$$\vec{\mathcal{E}}(\vec{r}; t) = f(z) [A_+(\vec{r}_\perp; t)\hat{e}_+ + A_-(\vec{r}_\perp; t)\hat{e}_-] e^{i\Omega t}, \quad (2.18)$$

where components and unitary vectors transform as

$$A_\pm = \frac{A_x \pm iA_y}{\sqrt{2}}, \quad \hat{e}_\pm = \frac{\hat{e}_x \mp i\hat{e}_y}{\sqrt{2}}. \quad (2.19)$$

A further step in the VCSEL modeling requires to introduce the material polarization which describe the interaction among the electric field and the active material. The evolution of the slowly-varying components of the material polarization \vec{P} , and the evolution of the carrier populations N_\pm can be determined using the density-matrix formalism [7] applied to a four level system. In absence of transverse effects, the polarization dynamics of a single longitudinal and transverse mode VCSEL is described by the spin flip model, which original equations read [13]

$$\dot{A}_\pm(t) = -\kappa A_\pm - ig_{QW} P_\pm - (\gamma_a + i\gamma_p) A_\mp + G_{A_\pm}(t), \quad (2.20a)$$

$$\dot{P}_\pm(t) = -\gamma_\perp(1 - i\theta) P_\pm + ig_{QW}(N \pm n) A_\pm + G_{P_\pm}(t), \quad (2.20b)$$

$$\dot{N}(t) = -\gamma(N - \sigma) + ig_{QW} [A_+^* P_+ + A_-^* P_- - \text{c.c.}] + G_N(t), \quad (2.20c)$$

$$\dot{n}(t) = -\gamma_s n + ig_{QW} [A_+^* P_+ - A_-^* P_- - \text{c.c.}] + G_n(t). \quad (2.20d)$$

A_\pm are the complex slowly-varying amplitudes of the electrical field, written in terms of the circular polarization components. P_\pm are the complex circular components of the material polarization that show a diagonal form only in this basis. $N \equiv (N_+ + N_-)/2$ is associated with the total population inversion between the conduction and valence bands and $n \equiv (N_+ - N_-)/2$ is the difference in population inversions of the two spin channels separately. The total population inversion decay with rate γ , while the differences in population inversions n relaxes with spin flip rate γ_s , introduced at this level as a phenomenological parameter. $\theta = (\omega_t - \Omega)/\gamma_\perp$ represents the normalized detuning of the gap transition frequency ω_t with respect to the longitudinal cavity mode resonance Ω . The material polarization decay rate is γ_\perp and the cavity decay rate is κ given in Eq. (1.3). g_{QW} stands for the effective coupling constant between the material dipole and the electric field given by Eq. (2.15). The pumping parameter σ is related to the injected current level.

The physical meaning of the different (deterministic) terms in Eqs. (2.20a)-(2.20d) follows from the general interpretation of rate equations. Eq. (2.20a) basically represents a balance between the material gain, provided by $\sim \text{Im} P_\pm$, and cavity losses; while the imaginary terms such as $\sim \text{Re} P_\pm$ induces a

non-linear frequency shift. The balance between the decay of material polarization and the excitation of dipoles (electron-hole pairs) due to the presence of an electric field is described through Eq. (2.20b). In Eq. (2.20c), the total carrier population increases due to current injection, and it decreases due to recombination of carriers, being either spontaneous or stimulated recombination. Finally, Eq. (2.20d) gives a detailed balance between the difference in number of stimulated recombination processes that take place in each spin channel separately; in addition, spin flip processes introduce a damping in this difference.

In a real situation the VCSEL structure is not perfectly symmetric under the interchange of the \hat{x} and \hat{y} directions due to, for instance, imperfections during the fabrication. This effect is accounted through the linear cavity anisotropies. The amplitude anisotropy γ_a is referred as dichroism while γ_p is the phase anisotropy or birefringence. The effect of the dichroism is to introduce different losses depending of the polarization orientation while birefringence introduces different refractive indexes. Several mechanisms contribute to birefringence: mechanical strain [14], linear electro-optic effect [15], and elasto-optic effect [16]. On the other hand, the application of strain in the QW plane introduces different gain for the two polarization components [17, 18]. The repercussion of these two important parameters, γ_a, γ_p , will be discussed in detail in the next section.

The terms $G_{A_{\pm}}, G_{P_{\pm}}, G_N, G_n$ represent semiclassical Langevin noise sources. $G_{P_{\pm}}$ model the quantum fluctuations of the photon-dipole interaction. From Sec. 2.1, we have that $\langle G_{P_{\pm}}(t)G_{P_{\pm}}^*(t') \rangle = \gamma_{\perp}(N \pm n)\delta(t-t')$, $N_{\pm} = (N \pm n)$ being the dipole number in each spin channel. Alternatively, $G_{P_{\pm}}$ can be expressed in terms of complex random numbers $\xi'_{\pm}(t)$, with zero mean $\langle \xi'_{\pm}(t) \rangle = 0$ and correlation $\langle \xi'_{\pm}(t)\xi'^*_{\pm}(t') \rangle = 2\delta(t-t')$ by means

$$G_{P_{\pm}}(t) = \sqrt{\frac{\gamma_{\perp}}{2}(N \pm n)} \xi'_{\pm}(t). \quad (2.21)$$

$\langle G_{A_{\pm}}(t)G_{A_{\pm}}^*(t') \rangle$ is proportional to the mean number of thermal photons that is negligible around $\lambda = 0.85\mu\text{m}$. G_N and G_n include among others, the pump fluctuations statistics and the shot noise from the time uncertainty in the recombination processes. We neglect these fluctuations, i.e., $\delta\sigma(t) = 0$; hence the non-vanishing Langevin sources are only $G_{P_{\pm}}$.

Spin-relaxation rate

A crucial parameter of the SFM in determining the polarization of the emitted light is the spin-relaxation time τ_s . Various spin-relaxation mechanisms in semiconductor QWs have been proposed, [19, 20, 21] and therein references: D'yakonov-Perel' (DP), Elliot-Yafet (EY), and Bir-Aronov-Pikus (BAP). In the DP process, the spin-orbit effect causes the splitting in energy of the conduction sub-bands that in conjunction with the lack of inversion symmetry causes

the re-orientation of the spins. In DP, $\tau_s \sim E_{1e}^{-2}$, with E_{1e} the first electron confinement energy in the QW. The EY process leads to spin-relaxation due to the mixing of the valence-band states into the conduction-band. Finally in BAP, the spin-flip appears as consequence of an interchange of scattering interaction between electrons and holes. In both EY and BAP processes, $\tau_s \sim E_{1e}^{-1}$, although the relative importance of BAP is significant only below 100K. The predictions of these models are contrasted with experimental determination of the spin-relaxation time. One possible way consists in optically pump the active media with circularly polarized pulses $p_{\pm}(t)$ and to analyze the circularly polarized emission. In the case of optical pumping, we neglect the stimulated recombination terms and we have

$$\frac{dN_{\pm}}{dt} = p_{\pm}(t) - \gamma N_{\pm} \mp \frac{1}{\tau_s} (N_+ - N_-), \quad (2.22)$$

since $n = (N_+ - N_-)/2$,

$$\frac{dn}{dt} = \frac{1}{2}(p_+(t) - p_-(t)) - \gamma_s n,$$

and $\gamma_s \equiv \gamma + 2\tau_s^{-1}$. From experiments, the main contribution to τ_s in GaAs QWs at room temperature is the DP process with typical values of $\tau_s \approx 40$ ps ($\gamma_s \approx 50$ ns⁻¹) for electron confinement energies around $E_{1e} = 100$ meV [21]. However, the most plausible candidate for the spin relaxation in InGaAs/InP QWs ($\lambda \approx 1.5\mu\text{m}$) at room temperature is the EY process due to their smaller band-gap. In this case, typical values at room temperature of $\tau_s \approx 5$ ps ($\gamma_s \approx 400$ ns⁻¹) for confinement electron energies $E_{1e} = 50$ meV [20] were found.

It is important to remark that γ_s correspond to the spin relaxation rate for electrons in the conduction band. Spin flip for holes is usually neglected, since sub-picosecond spin relaxation time is found at room temperature. The implications of a finite spin flip rate for electrons in the polarization properties of QW VCSELs will be discussed along this work.

Adiabatic elimination

From experimental measurements of the spin relaxation rate in QWs, the different rate constants in Eqs. (2.20a)-(2.20d) verify that

$$1\text{ns}^{-1} \sim \gamma \ll \gamma_s \lesssim \kappa \ll \gamma_{\perp} \sim 10^4\text{ns}^{-1}.$$

From this time scale analysis, we conclude that the material polarization correspond to the dynamical variable that relaxes with the faster time scale. Hence, it is justified to adiabatically eliminate the material polarization assuming that reaches nearly instantaneously its steady state, i.e., $\dot{P}_{\pm} \approx 0$ in Eq. (2.20b). In this limit, we obtain an expression for P_{\pm} that reads

$$P_{\pm}(t) \approx ig_{QW} \frac{(N \pm n)}{\gamma_{\perp}(1 + \theta^2)} (1 + i\theta) A_{\pm} + \frac{G_{P_{\pm}}(t)}{\gamma_{\perp}(1 - i\theta)}. \quad (2.23)$$

Upon replacing Eq. (2.23) in to the remaining equations, rescaling the dynamical variables by

$$D \equiv \frac{g}{\kappa} N, \quad d \equiv \frac{g}{\kappa} n, \quad g \equiv \frac{g_{QW}^2}{\gamma_{\perp}(1 + \theta^2)},$$

and performing a change of reference frame for the electric field from Ω to $\Omega + \kappa\theta$

$$E_{\pm} \equiv \sqrt{\frac{2g}{\gamma}} e^{-i\kappa\theta t} A_{\pm},$$

we arrive to the following rate equations describing the polarization dynamics of single longitudinal VCSELs in presence of spontaneous emission noise

$$\dot{E}_{\pm}(t) = \kappa(1 + i\alpha)[D \pm d - 1]E_{\pm} - (\gamma_a + i\gamma_p)E_{\mp} + F_{\pm}(t), \quad (2.24a)$$

$$\dot{D}(t) = -\gamma(D - \mu) - \gamma(D + d)|E_+|^2 - \gamma(D - d)|E_-|^2 - F_D(t), \quad (2.24b)$$

$$\dot{d}(t) = -\gamma_s d - \gamma(D + d)|E_+|^2 + \gamma(D - d)|E_-|^2 - F_d(t). \quad (2.24c)$$

A correct description of the sc dynamics requires to identify the normalized detuning θ with the linewidth enhancement factor of semiconductor lasers $\alpha \sim 2 - 4$. The α -factor is defined through

$$\alpha \equiv \frac{\partial_N \text{Im} \chi(\omega, N)}{\partial_N \text{Re} \chi(\omega, N)},$$

with $\chi(\omega, N)$ the optical susceptibility of the active material, $\tilde{P}_{\pm}(\omega) = \varepsilon_0 \chi(\Omega + \omega, N_{\pm}) \tilde{E}_{\pm}(\omega)$. The linewidth enhancement factor is the responsible of the phase-amplitude coupling and plays an important role in phase induced instabilities [22]. The rescaled injection current μ is such that at threshold $\mu_{th} \approx 1$. This reduced version of the SFM constitutes a non-linear system of 6 real ordinary differential equations (ODEs). In contrast to the traditional formulation of rate equations in EELs [4], in the SFM phase and amplitude variables can not be described separately, but they are directly coupled through the linear anisotropies and through the α -factor. The Langevin noise sources resulting from the adiabatic elimination of P_{\pm} read

$$F_{\pm}(t) = \sqrt{\beta_{sp}\gamma(D \pm d)} \xi_{\pm}(t), \quad (2.25a)$$

$$F_{(D)}(t) = \frac{\gamma}{2\kappa} \left[\sqrt{\beta_{sp}\gamma(D + d)} E_+ \xi_+^*(t) \pm \sqrt{\beta_{sp}\gamma(D - d)} E_- \xi_-^*(t) + c.c. \right]. \quad (2.25b)$$

$\xi_{\pm}(t)$ are two independent complex white noise terms with the same properties than $\xi'_{\pm}(t)$ in Eq. (2.21). The negative sign of the terms $F_{D,d}$ in Eqs. (2.24b) and

(2.24c) can be interpreted as the result of carrier burning when a spontaneous event of F_{\pm} takes place. In terms of the new variables, the rescaled fraction of spontaneously emitted photons that goes into the lasing mode reads

$$\beta_{sp} = \frac{\beta_0}{(1 + \alpha^2)} \frac{\kappa}{\gamma}. \quad (2.26)$$

Accordingly, the rescaled spontaneous emission rate is $R_{sp} = 4\gamma\beta_{sp}D_0$, $D_0 \sim 1$ being the degree of inversion. To get an impression of the magnitude of the rescaling, a noise level in the original equations of $\langle AA^* \rangle_{SQL} = 1/2$ corresponds to $\langle EE^* \rangle_{SQL} = \beta_0/(1 + \alpha^2) \approx 10^{-7}$ in the new variables.

2.3 Linearly-Polarized Solutions

We start our discussion, by analyzing the steady-state solutions of Eqs. (2.24a)-(2.24c). In particular, monochromatic linearly-polarized (LP) light can be expressed by

$$E_{\pm}(t) = Qe^{i(\omega t \mp \psi + \varphi_0)} \quad (2.27)$$

where Q is a real amplitude, ω is the nonlinear frequency shift with respect the longitudinal resonance Ω , ψ is an angle that describes the orientation of the LP states, and φ_0 is an arbitrary global phase for the electrical field. There exist two different solutions: a LP solution along the \hat{x} (\hat{y}) axis when $\psi = 0$ ($\psi = \pi/2$). Therefore, LP states can be regard as phase locking of the two circular components to a relative angle 2ψ . In addition, $D(t) = D_0$ and $d(t) = d_0$ in the steady state. Upon inserting these conditions in Eqs. (2.24a)-(2.24c), and neglecting the noise terms we find

$$\begin{aligned} \omega &= -\varepsilon(\gamma_p - \alpha\gamma_a), \\ D_0 &= 1 + \varepsilon\gamma_a/\kappa, \end{aligned} \quad (2.28)$$

$\varepsilon = 1$ (-1) when a \hat{x} (\hat{y})-LP solution is considered. In addition

$$\begin{aligned} Q^2 &= \frac{1}{2} \frac{(\mu - D_0)}{D_0}, \\ d_0 &= 0. \end{aligned} \quad (2.29)$$

The birefringence splits in frequency the two LP solutions, that are distanced the order of $2\gamma_p$. When $\gamma_p > 0$, \hat{x} (\hat{y}) is called the low (high) frequency mode. It is worth remarking that for a perfectly symmetric VCSEL, i.e., $\gamma_p = 0$ and $\gamma_a = 0$, any polarization orientation ψ provides a possible LP state.

2.4 Linearized Spin Flip Model

In this section, we present the equations governing the linearized dynamics close to an arbitrary LP solution. The resulting linear systems are the basis for the study of fluctuations in chapter 3. Moreover, a fundamental question is to understand the role of the spin flip in determining the stability of the LP solutions. The stability and fluctuations of a LP solution are studied by writing it as,

$$\begin{aligned} E_{\pm}(t) &= (Q + a_{\pm}(t))e^{i(\omega t \mp \psi)}, \\ D(t) &= D_0 + \Delta(t), \\ d(t) &= d_0 + \delta(t), \end{aligned} \quad (2.30)$$

with Q, ψ, D_0, d_0 given in Sec 2.3. a_{\pm} are complex perturbations of the electric field, while Δ and δ stand for real perturbations of the carrier variables. A linear stability analysis for the perturbed LP solutions provides a system of equations that decouple for the new variables, $S = a_+ + a_-$ and $R = a_+ - a_-$. The first subset, $\{S, S^*, \Delta\}$, describes the fluctuations of the total intensity

$$\begin{pmatrix} \dot{S} \\ \dot{S}^* \\ \dot{\Delta} \end{pmatrix} = \begin{pmatrix} 0 & 0 & \kappa(1+i\alpha)Q \\ 0 & 0 & \kappa(1-i\alpha)Q \\ -\gamma D_0 Q & -\gamma D_0 Q & -\gamma\mu/D_0 \end{pmatrix} \begin{pmatrix} S \\ S^* \\ \Delta \end{pmatrix}. \quad (2.31)$$

From this first subset, two eigenvalues determine the frequency and damping of the relaxation oscillations (ROs) that undergo the the total intensity, i.e., $\lambda_{\pm} = -\Gamma_R \pm i\Omega_R$. Their expressions are

$$\Gamma_R = \frac{\gamma\mu}{2D_0}, \quad \Omega_R^2 = 2\kappa\gamma(\mu - D_0) - \Gamma_R^2. \quad (2.32)$$

The remaining ³ eigenvalue is zero and it is associated with the arbitrariness in a global phase φ_0 , or equivalently, with the invariance in temporal translations.

The second subset, $\{R, R^*, \delta\}$, provides information about the polarization stability.

$$\begin{pmatrix} \dot{R} \\ \dot{R}^* \\ \dot{\delta} \end{pmatrix} = \begin{pmatrix} \pm 2(\gamma_a + i\gamma_p) & 0 & 2\kappa(1+i\alpha) \\ 0 & \pm 2(\gamma_a - i\gamma_p) & 2\kappa(1-i\alpha) \\ -\gamma D_0 Q & -\gamma D_0 Q & -(\gamma_s + 2\gamma Q^2) \end{pmatrix} \begin{pmatrix} R \\ R^* \\ \delta \end{pmatrix}. \quad (2.33)$$

An alternative way to study the polarization stability is to introduce the polarization orientation angle ϕ and the ellipticity angle χ through the real and imaginary parts of the complex amplitude difference $R(t)$

$$\delta\chi = \frac{R + R^*}{4Q}, \quad \delta\phi = i\frac{R - R^*}{4Q}.$$

³Note that under multitransverse mode operation additional RO frequencies of the total intensity associated with different transverse modes might appear [23].

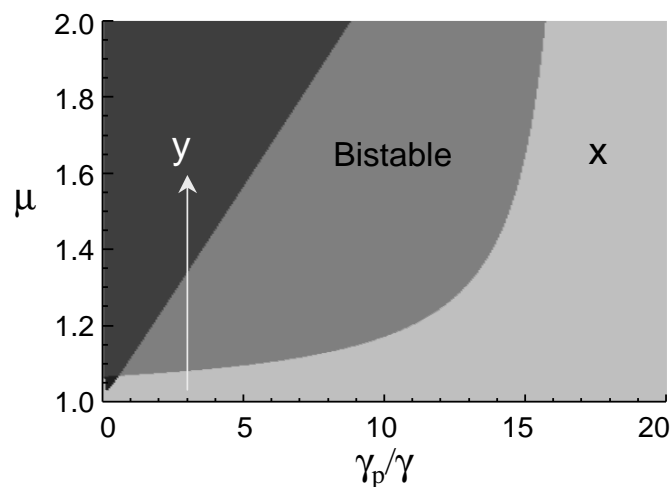


Figure 2.3: Linear stability of the linearly polarized solutions in the plane current-birefringence. The regions are: x-LP state stable (x), y-LP state stable (y), both states stable (bistable). The parameters are: $\alpha = 3$, $\gamma = 1 \text{ ns}^{-1}$, $\kappa/\gamma = 300$, $\gamma_a/\gamma = -0.1$, and $\gamma_s/\gamma = 100$.

In any case, the second subset provides a third order characteristic polynomial that reads

$$\begin{aligned} \mathcal{D}(\lambda) = & \lambda^3 + (\gamma_s + 2\gamma Q^2 \mp 4\gamma_a) \lambda^2 + \\ & 4 [\gamma_p^2 + \gamma_a^2 + \kappa\gamma Q^2 D_0 \mp \gamma_a (\gamma_s + 2\gamma Q^2)] \lambda + \\ & 4 [\gamma_p^2 + \gamma_a^2] (\gamma_s + 2\gamma Q^2) \mp 8\kappa\gamma Q^2 D_0 (\gamma_a + \alpha\gamma_p) . \end{aligned} \quad (2.34)$$

The signs $-$, $+$ are associated with the stability of \hat{x} , \hat{y} - LP states, respectively. $\mathcal{D}(\lambda) = 0$ determines the polarization stability, i.e., the state is unstable when there exists at least one eigenvalue with $\text{Re } \lambda > 0$, while the state is stable when $\text{Re } \lambda < 0$ for the three eigenvalues.

Polarization switching

Polarization switching (PS) takes place as consequence of a change in the stability of the polarization states, for instance, when increasing the injection current. Let us consider that $\gamma_a \lesssim 0$, therefore the \hat{x} -LP state has the lower threshold and it is selected when the current crosses the threshold. Both \hat{x} -LP and \hat{y} -LP states are stable below PS (coexistence region) except for currents close to threshold, due to the presence of γ_a . Increasing further the injection current, the \hat{x} -LP solution becomes unstable and a PS from the low frequency to the high frequency mode takes place. This type of switching, is successfully explained within the SFM [24, 25], and it is commonly referred as nonthermally induced PS since it occurs at constant active region temperature [26]. We remark that this type of switching is restricted to finite value of the spin flip rate γ_s , and non-vanishing α and γ_p . Another type of PS that is commonly present in experiments [14, 27, 28], namely, the thermally induced PS arises

from the temperature dependence of the gain difference between the two polarization states. An unified description of thermal and nonthermal induced PS has recently been introduced in terms of an extended SFM in [29, 30].

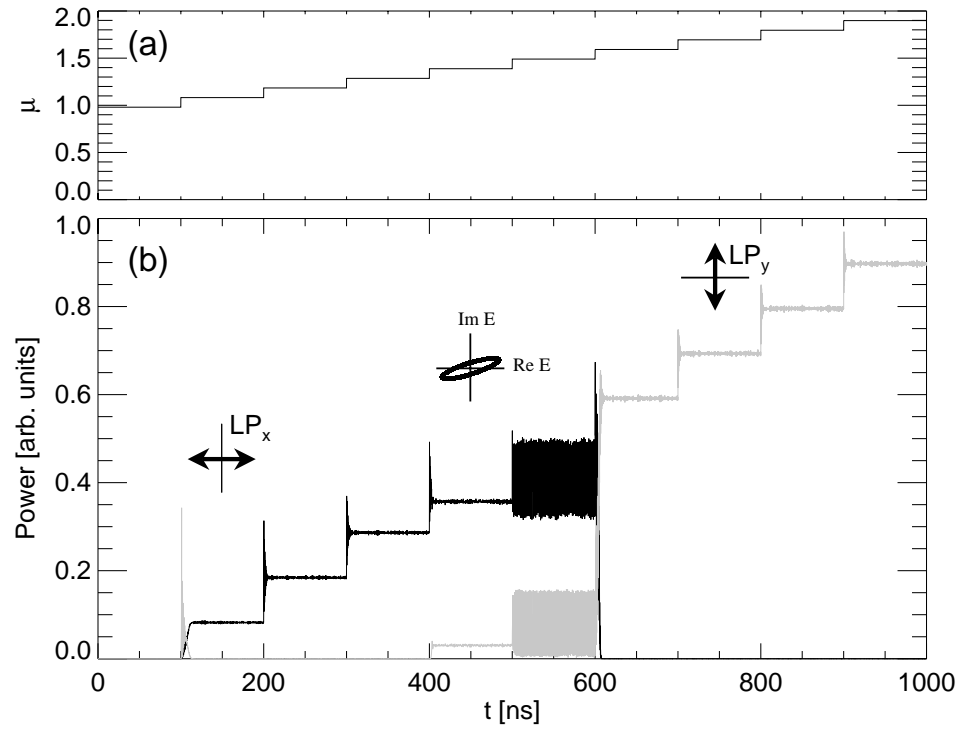


Figure 2.4: (a) Injection current increased in steps from below to above threshold. (b) Typical polarization switching from the low to the high frequency solution, taking place across elliptical and dynamical states. The same parameters than Fig. 2.3, except for $\gamma_p = 3 \text{ ns}^{-1}$.

Chapter 3

Semiclassical Analysis of Fluctuations

3.1 Introduction

MODE¹ partition noise (MPN) in semiconductor lasers [31] is detected by means of relative intensity noise (RIN) measurements and gives fundamental information on the dynamical properties of these devices. From the point of view of applications in optical communications, the degradation of the signal to noise ratio associated with MPN fixes limits on receiver sensitivity and bit error rates. Vertical-cavity surface-emitting lasers (VCSELs) operate on a single longitudinal mode, but multitransverse mode operation is common. MPN among these transverse modes and anticorrelated fluctuations of the modes have been described in different experiments and RIN measurements [32]-[41]. They have also been theoretically characterized [42, 43, 44]. The basic physical mechanism for this phenomenon is the same as for MPN among longitudinal modes of edge-emitting lasers, that is, spatial hole burning with modes competing for the same spatial carrier reservoir. The polarization of the light emitted by VCSELs is not as well stabilized as in edge-emitting lasers and VCSELs are known to have a number of polarization instabilities [24]. Transverse modes can have different polarization, but still MPN among different transverse modes is mostly caused by spatial effects.

A more subtle form of MPN occurs in VCSELs operating close to threshold. In this situation VCSELs lase in the fundamental transverse mode, but MPN arises from the competition of the two independent polarization components with essentially the same spatial profile. The effect of polarization fluctuations in the total intensity noise can significantly degrade the RIN characteristics [45] in a system with polarization sensitive elements. The importance of the fluctuations in the polarization component perpendicular to the dominant

¹This chapter is mainly based on the paper *Polarization resolved intensity noise in vertical-cavity surface-emitting lasers*. J. Mulet, C. R. Mirasso and M. San Miguel, Phys. Rev. A **64**, 023817 (2001).

one has been characterized in detail [46, 47, 48, 49]. Evidence of anticorrelated fluctuations of the two polarization components of the fundamental transverse mode has also been reported [49, 50] [See Fig. 3.1].

Due to their high quantum efficiency, low threshold, and single mode operation, VCSELs have been proposed as good candidates for the production of quantum squeezed light. In fact, production of squeezed light from VCSELs has been reported by several groups [35, 41, 51]. In this context an important question that has been addressed is the relevance of polarization partition noise (PPN) in degrading or achieving quantum squeezing [52].

A standard model for the study of polarization dynamics of VCSELs is the spin flip model (SFM), introduced in Chapter 2, and reduced versions of it [53]. Two important parameters of the model that enter in to the description of the dynamical coupling of the two polarization components are the cavity birefringence and the spin flip rate. The latter measures the direct coupling between the two groups of carriers with opposite spin that recombine into photons of opposite circular polarization. Previous studies of polarization fluctuations [46, 49, 52] take the SFM as a starting point. But, invoking the limit of fast spin flip rate and large birefringence, the SFM is reduced to a simple model with one degree of freedom or to the rate equations for a two-mode laser [31]. However, for VCSELs with small birefringence there is experimental evidence of the role of the nonlinear anisotropies associated with a finite spin flip rate. These effects are seen at least in three different characterizations of polarization fluctuations: A polarization type of four-wave mixing detected in the optical spectrum, polarization resolved intensity noise, and difference in the frequency splitting of the two polarizations at both sides of a polarization switching (PS) [46, 48]. In addition, and also for VCSELs with small birefringence, there is evidence of polarization switching [54] caused by phase-amplitude mechanisms of nonthermal origin described by the SFM [24, 25, 26, 29]. These results motivate the detailed analysis of the complete

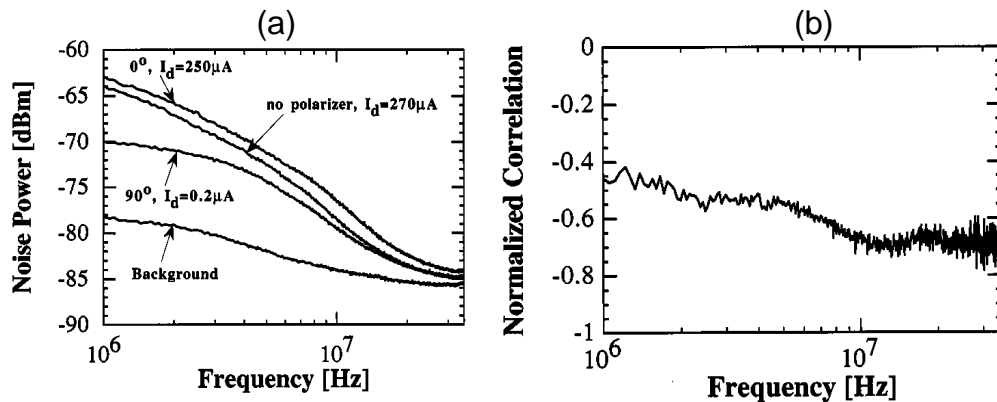


Figure 3.1: (a) Intensity noise of the $5\mu\text{m}$ device measured through a Glan-Thompson polarizer. (b) Normalized cross correlation between the two degenerate polarization modes in the $5\mu\text{m}$ device. Extracted from Ref. [50].

SFM presented here. Such analysis allows us to gain a full understanding of the dependence of polarization fluctuations on birefringence and spin flip rate in different ranges of values of these parameters.

In this work, we study the polarization resolved intensity noise of VCSELs operating in the fundamental transverse mode. We investigate the dynamical origin of anticorrelated polarization fluctuations. Such correlations emerge from mechanisms of polarization coupling and competition that are independent of spatial mode profiles. Anticorrelated dynamics of the polarization components also manifests itself in chaotic regimes caused by optical feedback [55]. We consider here the polarization dynamics within a semi-classical approach. This should give the necessary dynamical understanding for detailed studies of the quantum properties [56]. Our analysis focuses on the two circularly polarized components of the electric field. These are the natural variables for the nonlinear dynamics of an active semiconductor material. They are directly phase coupled by the cavity birefringence and also coupled through the carrier populations mixed by the spin flip. Focusing on the circularly polarized components, we are able to obtain explicit analytical expressions for their power spectra (in the approximation of linearized fluctuations). The competing roles of birefringence and spin flip rate become clear from these expressions. Our results for the circularly polarized components are discussed and compared with the polarization resolved spectra of the linearly polarized (LP) components obtained by a numerical analysis.

This chapter is organized as follows. In Sec. 3.2 we discuss the regimes with qualitative different dynamical operation in the SFM, associated with different values of anisotropies and spin flip. In Sec. 3.3 we present our results for the polarization resolved intensity noise for the circular and linear components on both sides of a polarization switch. In Sec. 3.4 we present the power spectra of the polarization fluctuations in the different regimes of operation. In Sec. 3.5 we discuss the role of birefringence and spin flip rate by visualizing the polarization fluctuations on the Poincaré sphere. In Sec. 3.6 we give a quantitative description of the anticorrelation of polarization fluctuations for circular and linear polarization components. We analyze the whole range of frequencies, from small frequency to frequencies beyond the relaxation oscillation frequency.

3.2 Regimes of Operation

The dynamical behavior, in the approximation of linear fluctuations, of any non-linear system is determined from the eigenvalues $\{\lambda_k\}$ and eigenvectors $\{\vec{\zeta}_k\}$ of the linearized system around a stable fixed point. Hence, we focus in regions where at least one linear polarization is stable, $\text{Re}\{\lambda_k\} \leq 0 \forall k$. Different domains of operation may be characterized by analyzing the eigenvalues and eigenvectors. For instance, a (negative) real eigenvalue determines

the damping of the relaxation while a pair of complex conjugated eigenvalues determine the damping and oscillation frequency. In turn, the associated eigenvectors determine the direction of faster contraction in the phase-space. In presence of fluctuations (noise), the understanding of the deterministic behavior is useful to interpret the noise spectra in each of these regions, as will be shown later.

A detailed analysis of the possible regimes of operation in the SFM has been described in [24, 57], discussing the effect of the spin flip relaxation rate, birefringence, and current injection. The behavior of the total intensity is already understood. From Eq. (2.32), we have oscillations at frequency Ω_R and damping rate Γ_R . Hence, the main issue is to understand the polarization behavior described by the linear system in Eq. (2.33). Despite of narrow regions where the polarization is unstable, and other ones without oscillations, two qualitative different situations arise². The first regime of operation, referred as polarization relaxation oscillations (PROs) [24], is favored in the case of small linear anisotropies. The second regime, referred as coupled oscillations (COs), tends to dominate for large spin flip rates. Proceeding along the lines described in [24], we summarize the behavior in each of these two regions. It is worth remarking that the asymptotic analysis, given in this section, provides the understanding of each region separately; however the way in which these two regions are connected is a matter of parameters. Some examples can be found in Fig. 3.2, where we represent the regimes of operation in the current vs. spin flip portrait for different situation of parameters.

A. Small linear anisotropies

We start our discussion describing the limit of small linear anisotropies. In this limit, the birefringence verifies that $\gamma_p \ll \gamma < \gamma_s < \kappa$, while for simplicity we take $\gamma_a = 0$. Note that $\gamma_a = \gamma_p = 0$ describes a perfectly symmetric VCSEL, i.e., any linear polarization direction is allowed. The eigenvalues of Eq. (2.34), $\mathcal{D}(\lambda) = 0$, can be expanded in power series of γ_p , that at first order read

$$\begin{aligned}\lambda_0 &= 2\varepsilon\alpha\gamma_p, \\ \lambda_{1,2} &= \lambda_{1,2}^o - \varepsilon \frac{\alpha\gamma_p}{1 + \frac{\gamma_s + 2\gamma Q^2}{8\kappa\gamma Q^2} \lambda_{1,2}^o},\end{aligned}\tag{3.1}$$

²The limits $\kappa \gg \gamma, \gamma_p, \gamma_s$ and $\gamma \sim \gamma_s \gg \kappa, \gamma_p$ also correspond to qualitative different regimes; however being unusual in sc lasers. In both cases the typical time scales for the decay of the electric field κ and those for the carrier variables γ, γ_s decouple. Consequently, the exchange of energy between the two subsystems is unfavored avoiding the appearance of oscillations.

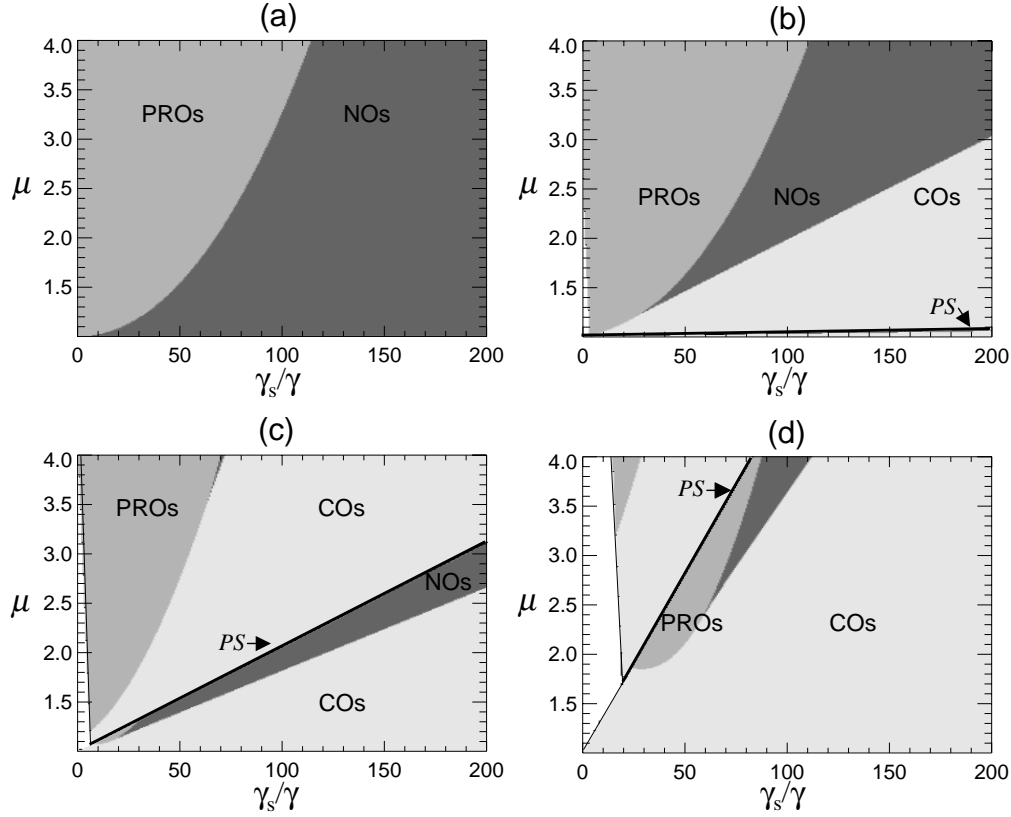


Figure 3.2: Regions of operation represented in the phase diagram current vs. spin flip. The parameters are: $\alpha = 3$, $\gamma = 1 \text{ ns}^{-1}$, $\kappa/\gamma = 300$, $\gamma_p = \gamma_a = 0$ in panel (a). $\alpha = 3$, $\gamma = 1 \text{ ns}^{-1}$, $\kappa/\gamma = 300$, $\gamma_p/\gamma = 0.5$, $\gamma_a/\gamma = -0.1$ in panel (b). $\alpha = 1$, $\gamma = 1 \text{ ns}^{-1}$, $\kappa/\gamma = 150$, $\gamma_p/\gamma = 3$, $\gamma_a/\gamma = -0.1$ in panel (c). $\alpha = 1$, $\gamma = 1 \text{ ns}^{-1}$, $\kappa/\gamma = 150$, $\gamma_p/\gamma = 10$, $\gamma_a/\gamma = -0.1$ in panel (d). Meaning of the symbols: Polarization relaxation oscillations (PROs), coupled oscillations (COs), absence of polarization oscillations (NOs), polarization switching current from LF to HF solution (PS). Note also narrow white regions where no linearly polarized solution is stable.

with $\varepsilon = \pm 1$ for \hat{x}, \hat{y} -LP solutions. $\lambda_{1,2}^o$ are the two non-vanishing eigenvalues calculated at $\gamma_p = 0$

$$\lambda_{1,2}^o = -\frac{\gamma_s + 2\gamma Q^2}{2} \pm i\sqrt{4\kappa\gamma Q^2 - \frac{(\gamma_s + 2\gamma Q^2)^2}{4}}.$$

In the absence of birefringence, the eigenvalue $\lambda_0 = 0$ is associated with the arbitrariness in the polarization orientation. In the presence of small birefringence, this real eigenvalue becomes non-zero determining the stability of the high frequency solution. The eigenvector associated with λ_0 lies in the direction of the polarization orientation and decouples of the fluctuations of the ellipticity and carrier difference $d(t)$. The remaining eigenvalues $\{\lambda_{1,2}\}$ are complex when

$$\gamma_s < \gamma_s^c \equiv \sqrt{8\kappa\gamma(\mu - 1)} - \gamma(\mu - 1),$$

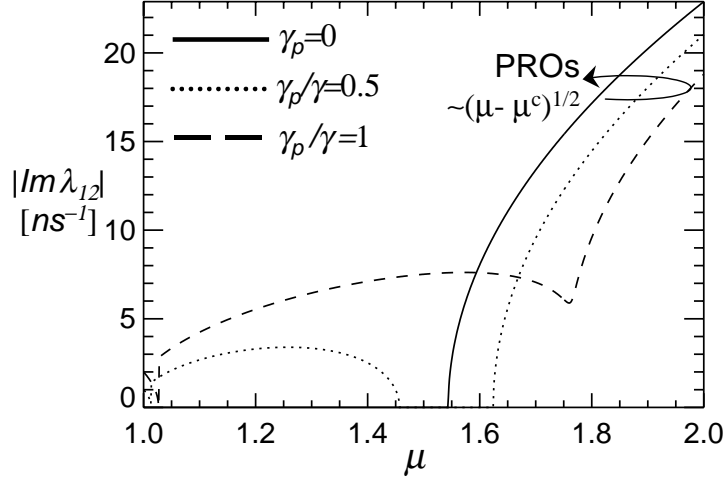


Figure 3.3: Evolution of the effective birefringence as function of the injection current in the limit of small linear anisotropies. Polarization relaxation oscillations (PROs) dominate the dynamical behavior at high injection currents. Since polarization switching occurs very close to threshold $\mu \approx 1$, the effective birefringence corresponds to the stable high frequency solution (\hat{y}). Parameters: $\gamma = 1 \text{ ns}^{-1}$, $\alpha = 3$, $\kappa/\gamma = 300$, $\gamma_a = 0$, and $\gamma_s/\gamma = 50$.

which implies small to moderate values of γ_s and currents relatively far from threshold. In such a case, $|\text{Im}\lambda_{1,2}|$ describes the oscillation frequency that undergo the ellipticity angle and $d(t)$, known as *polarization relaxation oscillations* (PROs). Fig. 3.3 depicts the evolution of the imaginary part of the eigenvalues $\lambda_{1,2}$, for small values of the birefringence, when the current is increased from threshold. Similarly to ROs, the PROs frequency grows with the square-root of the distance to its threshold, $\sim (\mu - \mu^c)^{1/2}$. Finally, for larger spin flip, $\gamma_s > \gamma_s^c$, the polarization fluctuations experience damped relaxation without any kind of oscillation.

B. Large spin flip rate. Non-linear anisotropies

Another interesting limit is when the spin flip relaxation rate is large, i.e, $\gamma < \gamma_p < \kappa \ll \gamma_s$. There exist two complex eigenvalues and a real one. The real eigenvalue is $\lambda_0 \approx -\gamma_s$ and describes the damped relaxation of $d(t)$. The two complex conjugated eigenvalues of Eq. (2.34), are expanded in power series of γ_s^{-1} . They have two different contributions

$$\lambda_{1,2} = \lambda_{lin} + \lambda_{non}.$$

The linear contribution, arising in the limit³ of $\gamma_s = \infty$, is $\lambda_{lin} = 2\varepsilon\gamma_a \pm i2\gamma_p$ and represents oscillations whose damping and frequency are exclusively determined by the linear anisotropies. The non-linear contribution λ_{non} is the

³We note that the same result for λ_{lin} is obtained close to threshold, where Q^2 is treated as a small parameter, regardless of the magnitude of γ_s .

result of a finite value of γ_s . It is common to define the non-linear dichroism and non-linear birefringence [47] as the real and imaginary parts of λ_{non} , i.e. $\lambda_{non} = \gamma_{non} \pm i\omega_{non}$. Finally, the two complex eigenvalues read

$$\lambda_{1,2} = 2\varepsilon\gamma_a \pm i2\gamma_p - \frac{1}{\gamma_s}\gamma\kappa(\mu - D_0) [1 \pm i\alpha\varepsilon \text{sign}(\gamma_p)] . \quad (3.2)$$

The imaginary part of these eigenvalues describes *coupled oscillations* (COs) of the polarization angles. The approximate expression for the COs frequency in the limit of large γ_s is then

$$\Omega_P \equiv |\text{Im}\lambda_{1,2}| = 2|\gamma_p| \mp \frac{\gamma}{\gamma_s}\alpha\kappa(\mu - D_0) + o\left(\frac{\gamma}{\gamma_s}\right)^2, \quad (3.3)$$

where Ω_P decreases (increases) for the LF (HF) mode corresponding to the sign $-(+)$. In contrast to ROs and PROs, the COs frequency varies linearly with the distance to threshold, i.e. $\sim (\mu - 1)$. From the last expression, the Ω_P frequency⁴ can be identified with the birefringence splitting γ_p although modified by the nonlinearities and the spin flip rate. It can be seen that the nonlinear anisotropies obtained from the adiabatic elimination of $d(t)$ [47, 48] coincide, at first order in γ/γ_s , with those predicted by Eq. (3.2). Consequently, these previous works, based on the adiabatic elimination of $d(t)$ are unsuitable to describe the dynamical properties within the PROs region we have described before. In contrast to PROs, where $\text{Re}\lambda_0 < 0$ determines the stability, the stability of the LP solutions is now determined by the complex eigenvalues with $\text{Re}\lambda_{1,2} < 0$. At threshold and in presence of dichroism, only the HF polarization is stable. Increasing the injection current, the role of γ_{non} is to stabilize the non-lasing polarization component and increase the damping of the lasing one.

In the limit of the adiabatic elimination of $d(t)$, polarization switching is not present. When analyzing the real part of the eigenvalues Eq. (3.2), we go from a situation where only one polarization is stable to one of optical bistability when the current is increased. Polarization switching occurs for moderate values for γ_s , reflecting itself in the expression of γ_{non} when orders $(\gamma/\gamma_s)^2$ are considered. Hence, in this work, we deal with the dynamics of $d(t)$ being capable to describe, without any restriction, the fluctuations in both PROs and COs regimes. When restricting the analysis to moderate values of γ_s , we observe in Fig. 3.4 that Eq. (3.2) still provides the qualitative evolution for the real and imaginary parts of the eigenvalues $\lambda_{1,2}$. However, a polarization switching (PS) from the low frequency to the high frequency solution is observed at finite injection currents. As a consequence, the effective birefringence increases with a discontinuity at the PS current.

⁴ Ω_P is also referred as effective birefringence splitting.

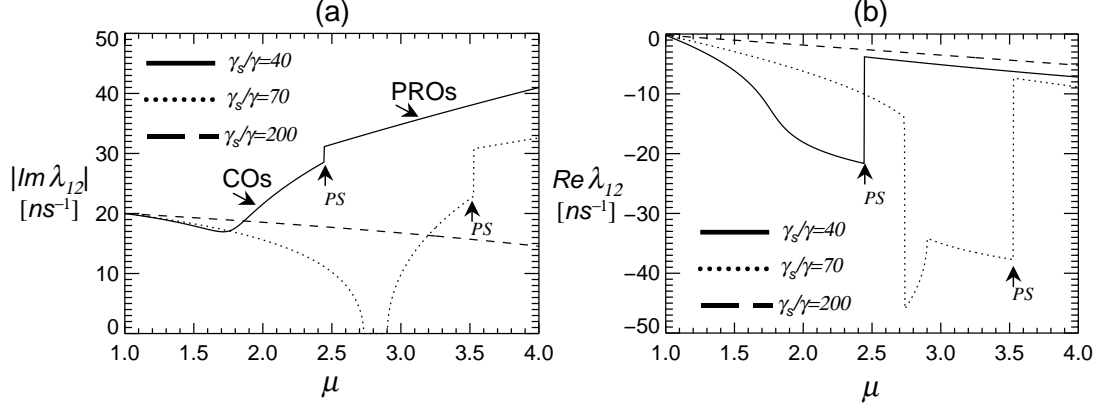


Figure 3.4: Effective birefringence (a) and effective dichroism (b) as function of the injection current for three different spin flip rates. PS denotes the position of the polarization switching. Below PS we consider a low frequency LP solution, while above PS only the high frequency solution is stable. For small γ_s and below PS, a transition from COs to PROs takes place. Above PS and for large γ_s the dynamical behavior is dominated by COs. Parameters: $\gamma = 1 \text{ ns}^{-1}$, $\alpha = 1$, $\kappa/\gamma = 150$, $\gamma_a/\gamma = -0.1$, and $\gamma_p/\gamma = 10$.

Optical spectrum of the non-lasing component

The physical interpretation of the non-linear anisotropies becomes evident when analyzing the frequency splitting between lasing and non-lasing components of a LP solution. For instance, let us consider fluctuations around a stable \hat{x} -LP solution. The circular components of the optical field read

$$E_{\pm}(t) = [Q + a_{\pm}(t)] e^{i\omega_x t},$$

with $\omega_x = -\gamma_p + \alpha\gamma_a$ being the frequency of the lasing \hat{x} -component. Thus, the non-lasing component of the electric field reads

$$E_y(t) = \frac{-i}{\sqrt{2}} [a_+(t) - a_-(t)] e^{i\omega_x t} \sim R(t) e^{i\omega_x t},$$

with $R(t)$ being solution of Eq. (2.33) by proper addition of Langevin noise terms⁵. For the sake of simplicity and without loss of generality, we assume that the characteristic polynomial associated with $R(t)$ have a real eigenvalue λ_0 and two complex conjugated $\lambda_{1,2} \equiv \lambda_c$ eigenvalues, as those described in Sec. 3.2B.

A general solution of Eq. (2.33), to a perturbation applied at $t = 0$, can be written as

$$E_y(t) = [Ae^{\lambda_0 t} + (Be^{i\text{Im}\lambda_c t} + Ce^{-i\text{Im}\lambda_c t})e^{\text{Re}\lambda_c t}] e^{i\omega_x t}. \quad (3.4)$$

with A, B, C integration constants to be determined from the initial condi-

⁵For a description of the optical spectra in VCSELs see for instance [58]

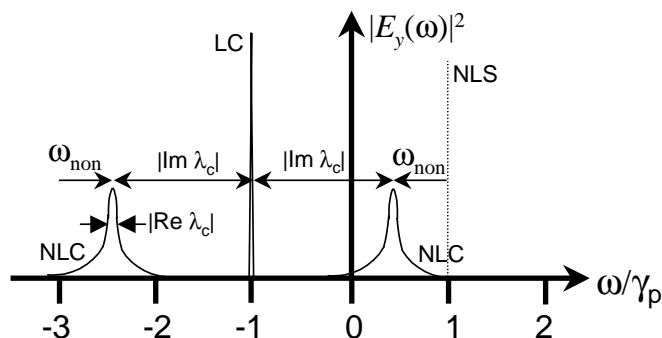


Figure 3.5: Schematic representation of the optical spectra of the lasing (LC) and non-lasing components (NLC) of the electric field. NLS denotes the position of the orthogonal lasing solution. The meaning of the other symbols is discussed in the text.

tions. The optical spectrum is obtained by Fourier transforming Eq. (3.4)

$$|\tilde{E}_y(\omega)|^2 \sim \frac{1}{[(\omega - \omega_x)^2 + \lambda_0^2]} \times \frac{1}{[(\omega - \omega_x - |\text{Im}\lambda_c|)^2 + (\text{Re}\lambda_c)^2][(\omega - \omega_x + |\text{Im}\lambda_c|)^2 + (\text{Re}\lambda_c)^2]}, \quad (3.5)$$

The optical spectrum of the non-lasing component (\hat{y}), represented in Fig. 3.5, displays two peaks symmetrically located around ω_x and distanced by $2|\text{Im}\lambda_c|$. In the absence of non-linear anisotropies, for instance close-to-threshold or for very large γ_s , one of these peaks is located at the position of the orthogonal lasing solution. As soon as the non-linearities start to play a role, the non-lasing peaks approach one to each other by an order of $2\omega_{non}$. Finally, when $|\text{Im}\lambda_c| = 0$ lasing and non-lasing component fluctuations merge into a single peak located at the lasing frequency ω_x . This last stage is usually linked to the appearance of elliptic states followed by a polarization switching [25].

3.3 Fluctuation of the Intensity Components

In order to better understand the intensity fluctuations of the polarization components, Eqs. (2.24a)-(2.24c) can be translated from the field description $E_{\pm}(t)$ to equations for the circular intensities $P_{\pm}(t)$ and the phase difference $\phi(t) \equiv \phi_+(t) - \phi_-(t)$ through $E_{\pm}(t) = \sqrt{P_{\pm}(t)}e^{i\phi_{\pm}(t)}$. The stochastic transforma-

tion in the Itô sense [Appendix B] of Eqs. (2.24a)-(2.24c) reads

$$\begin{aligned} \dot{P}_{\pm}(t) &= 2\kappa[D \pm d - 1]P_{\pm} - 2\sqrt{P_+P_-}[\gamma_a \cos \phi \pm \gamma_p \sin \phi] \\ &\quad + 2\beta_{sp}\gamma[D \pm d] + F_{P_{\pm}}(t), \end{aligned} \quad (3.6a)$$

$$\begin{aligned} \dot{\phi}(t) &= 2\kappa\alpha d - \sqrt{\frac{P_-}{P_+}}[\gamma_p \cos \phi - \gamma_a \sin \phi] + \sqrt{\frac{P_+}{P_-}}[\gamma_p \cos \phi + \gamma_a \sin \phi] \\ &\quad + F_{\phi}(t), \end{aligned} \quad (3.6b)$$

$$\dot{D}(t) = -\gamma(D - \mu) - \gamma(D + d)P_+ - \gamma(D - d)P_- - F_D(t), \quad (3.6c)$$

$$\dot{d}(t) = -\gamma_s d - \gamma(D + d)P_+ + \gamma(D - d)P_- - F_d(t), \quad (3.6d)$$

with the Langevin terms

$$F_{P_{\pm}} = \sqrt{4\beta_{sp}\gamma(D \pm d)P_{\pm}} \xi_{P_{\pm}}, \quad (3.7a)$$

$$F_{\phi} = \sqrt{\frac{\beta_{sp}\gamma(D + d)}{P_+}} \xi_{\phi_+} - \sqrt{\frac{\beta_{sp}\gamma(D - d)}{P_-}} \xi_{\phi_-}, \quad (3.7b)$$

$$F_{(D/d)} = \frac{\gamma}{\kappa} \left[\sqrt{\beta_{sp}\gamma(D + d)P_+} \xi_{P_+} \pm \sqrt{\beta_{sp}\gamma(D - d)P_-} \xi_{P_-} \right], \quad (3.7c)$$

$\xi_{P_{\pm}}, \xi_{\phi_{\pm}}$ being real white Gaussian random numbers with zero mean and correlation $\langle \xi_a(t)\xi_b(t') \rangle = \delta_{a,b}\delta(t - t')$.

In order to calculate the power fluctuations of the total intensity and circular components, we linearize Eqs. (3.6a)-(3.6d) around their steady states. We have $P_{\pm 0} = Q^2$, $d_0 = 0$, and $D_0 = 1 \pm \gamma_a/\kappa$ when $\phi_0 = 0, \pi$. For convenience, we calculate the fluctuations for the total intensity $\delta P(t) = \delta P_+(t) + \delta P_-(t)$ and the intensity difference $\delta q(t) = \delta P_+(t) - \delta P_-(t)$. The linearized equations can be straightforwardly solved via Fourier transform, yielding the expressions

$$\tilde{\delta P}(\omega) = \sqrt{2Q^2R_{sp}} \frac{[i\omega + \gamma] \tilde{\xi}_P}{[\omega - \Omega_R + i\Gamma_R][\omega + \Omega_R + i\Gamma_R]}, \quad (3.8a)$$

$$\begin{aligned} \tilde{\delta q}(\omega) &= \sqrt{2Q^2R_{sp}} \times \\ &\quad \frac{[\varepsilon 4\alpha Q^2 \gamma \gamma_p + (i\omega - \varepsilon 2\gamma_a)(\gamma_s + i\omega)] \tilde{\xi}_q - \varepsilon 2\gamma_p (\gamma_s + 2\gamma Q^2 + i\omega) \tilde{\xi}_{\Phi}}{\mathcal{D}(i\omega)}, \end{aligned} \quad (3.8b)$$

where Γ_R and Ω_R are given by Eq. (2.32) and $\mathcal{D}(\lambda)$ is given by Eq. (2.34); $\varepsilon = 1(-1)$ stands for a $\hat{x}(\hat{y})$ LP solution. The Fourier transformed noise sources $\tilde{\xi}_P(\omega)$, $\tilde{\xi}_q(\omega)$ and $\tilde{\xi}_{\Phi}(\omega)$ verify that $\langle \tilde{\xi}_i(\omega)\tilde{\xi}_j(\omega') \rangle = \delta_{i,j} \delta(\omega - \omega')$ for $i, j = P, q, \Phi$.

Power spectra of the total and difference intensities can be straightforwardly derived from its definition in Eq. (2.11)

$$S_P(\omega) = \int_{-\infty}^{\infty} \langle \tilde{\delta P}(\omega)\tilde{\delta P}^*(\omega') \rangle d\omega',$$

and from Eqs. (3.8a)-(3.8b) yielding

$$S_P(\omega) = 2Q^2 R_{sp} \frac{(\omega^2 + \gamma^2)}{[(\omega - \Omega_R)^2 + \Gamma_R^2][(\omega + \Omega_R)^2 + \Gamma_R^2]}, \quad (3.9a)$$

$$S_q(\omega) = 2Q^2 R_{sp} \frac{(\mathcal{A}_\chi(\omega) + \mathcal{B}_\chi(\omega))}{\mathcal{C}(\omega)}. \quad (3.9b)$$

The functions $\mathcal{A}_\chi, \mathcal{B}_\chi, \mathcal{C}$ are given in Appendix A and $R_{sp} = 4\gamma\beta_{sp}D_0$. We note that the relative intensity noise is defined as the power spectrum divided by the square of the mean value of the total power, $\bar{P}^2 = (2Q^2)^2$.

The power spectrum of the circular components $S_\pm(\omega)$ can be obtained from Eqs. (3.9a) and (3.9b) by taking into account that the noise terms appearing in the fluctuations $\delta\tilde{P}(\omega)$ and $\delta q(\omega)$ are independent,

$$\delta P_\pm \equiv \frac{\delta P \pm \delta q}{2}, \quad S_+(\omega) = S_-(\omega) = \frac{S_P(\omega) + S_q(\omega)}{4}. \quad (3.10)$$

It is important to remark that the contribution to the noise of the circular components arises from the linear superposition of the total intensity noise S_P and the polarization fluctuations S_q . This separation is possible in LP states because the total intensity fluctuations and the intensity difference fluctuations decouple (at first order). However, for other states (elliptical [59] and dynamical states [25]) the decoupled description is not valid requiring, in principle, the study of a five-dimensional system.

Let P_u and P_v be the power of each orthogonal component ($u = +, v = -$ for the circular components, or alternatively $u = x, v = y$ for the linear components). Since the fluctuation of the total intensity is a scalar we can express it in any of the two basis

$$\delta P = \delta P_+ + \delta P_- = \delta P_x + \delta P_y.$$

However, this result does not hold for the power spectra. Instead one finds

$$S_P(\omega) = S_u(\omega) + S_v(\omega) + \int_{-\infty}^{\infty} 2\text{Re}\langle \delta\tilde{P}_u(\omega)\delta\tilde{P}_v^*(\omega') \rangle d\omega'. \quad (3.11)$$

In the particular case of the circular components and making use of Eq. (3.10) we obtain

$$\text{Re} \int_{-\infty}^{\infty} \langle \delta\tilde{P}_+(\omega)\delta\tilde{P}_-(\omega') \rangle d\omega' = \frac{S_P(\omega) - S_q(\omega)}{4}, \quad (3.12)$$

which implies that the fluctuations of the circular components $\delta P_+, \delta P_-$ are correlated when $S_P(\omega) > S_q(\omega)$, anticorrelated when $S_P(\omega) < S_q(\omega)$ and uncorrelated where $S_P(\omega) = S_q(\omega)$. In the Sec. 3.6 we will insist on the correlation between polarization components.

In this section we present analytical and numerical results of the polarization resolved intensity noise. Since the circular basis is the natural basis to study the optical transitions, we start investigating the power fluctuations of the circular components followed by the power spectra of the linear components for LP states when crossing a nonthermal polarization switching. We consider the situation where $d(t)$ relaxes exponentially with time constant γ_s^{-1} while coupled oscillations (COs) of the ellipticity and polarization orientation appear at frequency Ω_P .

Fluctuations of the circular components

Two mechanisms are responsible for the coupling between dynamical variables. On one hand, the carriers with spin up and down are coupled through the spin flip rate, and the limits $\gamma_s \rightarrow \infty$ and $\gamma_s \rightarrow 0$ correspond to the fast spin relaxation and slow spin relaxation rate, respectively. The second mechanism is the birefringence. Microscopically, the birefringence transforms left polarized photons into right ones and vice versa. The macroscopic effect is to provide LP states with a well defined polarization orientation. Therefore, we expect that both the spin flip rate and the birefringence play an important role in the origin of noise anticorrelations of the polarized components. Finally, dichroism introduces different losses between the two LP states, selecting the mode with highest (unsaturated) gain at threshold. Experimental determination of fluctuations of the circular components can be performed by using $\lambda/4$ plate techniques [47]. We concentrate our study on finite values of the spin flip rate and relatively small birefringence which corresponds to COs regime. We investigate the power spectra for different values of the spin flip rate and birefringence while maintaining the rest of the laser parameters fixed. The dichroism is set to $\gamma_a \lesssim 0$ in order to select the low frequency mode (\hat{x}) at threshold. A nonthermal PS takes place from the low frequency mode (\hat{x} -LP) to the high frequency one (\hat{y} -LP) when the injection current is increased.

In Fig. 3.6 we plot the power spectra obtained for $\gamma_s = 100 \text{ ns}^{-1}$, $\gamma_p = 1 \text{ ns}^{-1}$; $\mu = 1.04 < \mu_{sw}$ in panels 3.6(a,b), while $\mu = 1.5 > \mu_{sw}$ in panels 3.6(c,d). Analytical results obtained from Eqs. (3.9a) and (3.10) are plotted in Fig. 3.6(a,c) with solid thin lines. As can be seen, they are in very good agreement with the numerical results. The spectrum of the total intensity has a single peak located at the relaxation oscillation frequency $\nu_R = \Omega_R/(2\pi)$. This peak is due to fluctuations in the total photon number. In contrast, the power spectra of the circular components coincide and display an additional peak at the CO frequency ν_P , which moves toward γ_p/π when $\gamma_s \rightarrow \infty$, in agreement with Eq. (3.3). We note that the height of the CO peak is larger and it appears at lower frequency before the PS, in qualitative agreement with Ref. [47]. It can be clearly seen that the noise in the two circular components is much larger than the total intensity noise at low frequencies, a sign of anticorrelation between

δP_+ and δP_- . This anticorrelation is interrupted at higher frequencies due to the peak associated with the fluctuations in the total intensity. In fact, we find maximum correlation at ν_R , as will be discussed later.

Fluctuation of the linear components

When a LP state is considered, there is a linear component that captures nearly the total intensity (lasing component), with mean power level \bar{P}_l , and one with very small intensity (nonlasing component) with \bar{P}_{nl} . Although a LP state is considered, we find that fluctuations in the nonlasing component are relevant. On the other hand, we have shown that the circular components phase-lock to a relative phase $\phi = \phi_+ - \phi_-$. However, phase-locking among linear components is not possible because they operate at different frequency due to birefringence. By expressing the linear components of the electric field through $E_{x,y} = \sqrt{P_{x,y}}e^{i\phi_{x,y}}$, the relative phase $\phi_x - \phi_y$ evolves at a typical time scales of $\sim 2\gamma_p$. It is then possible that by invoking the limit of large γ_p to eliminate the information carried by the phase dynamics and to reduce the SFM to equations describing a two-mode laser [46, 52].

It is illustrative to analyze the way in which the fluctuations are distributed among different polarization components. The probability density

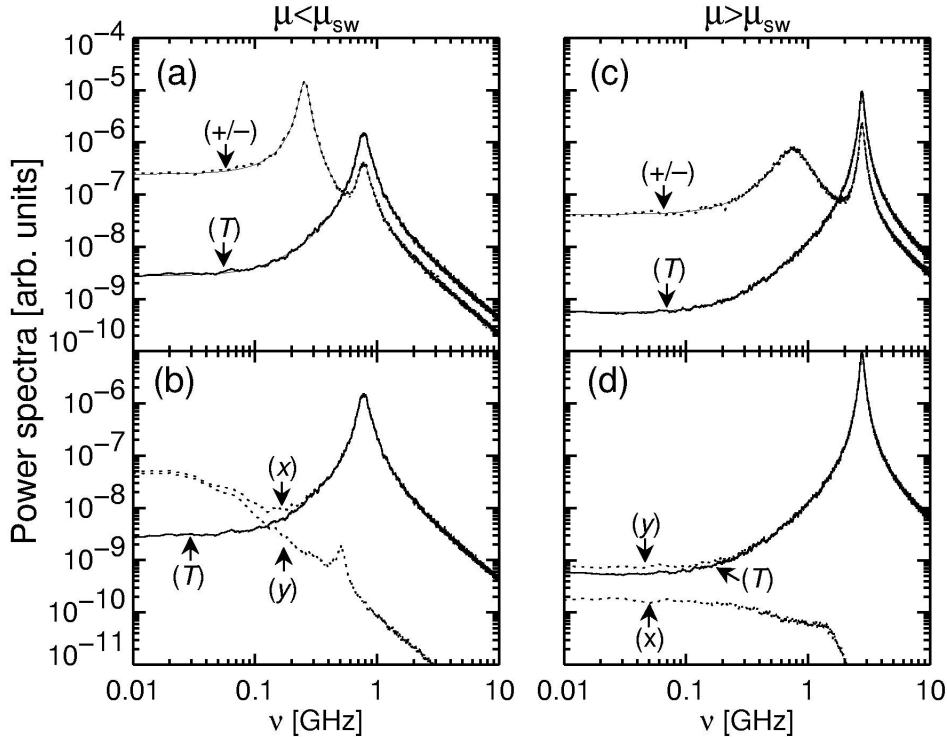


Figure 3.6: Power spectra in arbitrary units for currents below PS (a,b), and above PS (c,d). Solid thin lines in (a) and (c) represent the theoretical predictions given by Eqs. (3.9a) and (3.10). Parameters: $\gamma = 1 \text{ ns}^{-1}$, $\kappa/\gamma = 300$, $\alpha = 3$, $\gamma_p/\gamma = 1$, $\gamma_s/\gamma = 100$ and $\beta_{sp} = 10^{-5}$.

function (PDF) of a intensity component P is computed through

$$p.d.f(P_0) \approx \frac{\mathcal{P}[P_0 < P < P_0 + dP_0]}{dP_0},$$

where $\mathcal{P}[P_0 < P < P_0 + dP_0]$ is the probability that the intensity takes the values within the interval $[P_0, P_0 + dP_0]$. We approximate this quantity by the fraction of data points within $[P_0, P_0 + dP_0]$, i.e. $\mathcal{N}[P_0 < P < P_0 + dP_0]/N$. The PDF of circular components $p.d.f(P_{\pm})$, in Fig. 3.7(b), coincides and display a Gaussian shape with a maximum around its mean value. In the same panel, we plot the PDF associated with the total intensity that is also Gaussian but with narrower width as a result of anticorrelated fluctuations between circular components [See Fig. 3.7(a)]. The PDF of the lasing component, in panel (d), and the total intensity are similar. Hence, the fluctuations of the total intensity, circular components, and the lasing component can be described by Ornstein-Uhlenbeck stochastic equations, which their associated Fokker-Planck equations have Gaussian distributions as stationary solutions. However, we observe in Fig. 3.7(c) that the fluctuations of the non-lasing component prefer intensity levels lower than the mean value. In addition, the associated PDF displays a single-sided exponential decay, like that of “thermal” fluctuations.

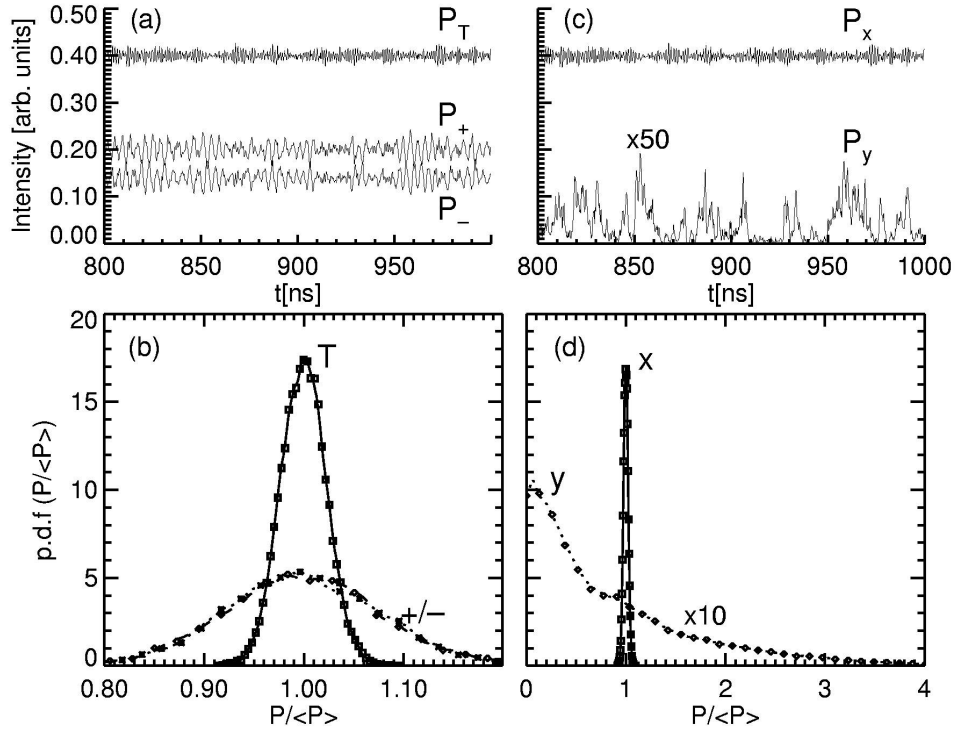


Figure 3.7: (a) Temporal trace of the total intensity P_T and the circular components P_{\pm} . Note that the P_- has been vertically shifted to aid the eye. (b) Probability density function (PDF) for P_T, P_{\pm} . (c) Temporal trace of the lasing P_x and nonlasing fluctuations P_y . (d) Probability density function (PDF) for P_x, P_y . The same parameters as in Fig. 3.6(a,b).

The power spectrum of the total intensity and the linear lasing component has a peak located at the RO frequency, as can be seen in Fig. 3.6(b, d). However, the CO peak is not present in this case. While the lasing component captures nearly all the noise at high frequency, the power spectrum of the nonlasing component has a small peak close to the frequency beating between Ω_R and Ω_P . The power spectrum of the nonlasing component has a small contribution to the total noise at high frequencies, displaying a clear Lorentzian decay [49]. The power spectrum of the total intensity results from the superposition of the fluctuations of the lasing and non-lasing components. The behavior at low frequencies requires a more subtle study. The noise in the two polarization components can exceed the total noise by several orders of magnitude at low frequencies. This particular behavior occurs in LP states with important fluctuations in the polarization orientation, yielding relative high values of the parameter $M \equiv \overline{P}_{nl}/\overline{P}_l$. Below the PS, in the coexistence regime, strong anticorrelated fluctuations appear at low frequencies [Fig. 3.6(b)]. On the contrary, above the PS, M decreases and anticorrelation nearly vanishes as can be seen in Fig. 3.6(d). A possible interpretation of polarization anticorrelations will be given in Sec. 3.5 in terms of the carrier reservoirs. PPN has been claimed to be sensitive to the parameter M [31]. An approximate expression for M can be determined from a one-dimensional version of the SFM based on a high-friction or low mass limit Kramers' problem. In this limit, the expression for M reads [47]

$$M \sim \frac{\gamma_s \beta_{sp}}{\kappa(\mu - D_0)},$$

which tells that the noise in the non-lasing component increases when the noise strength is increased, when the operation is restricted close-to-threshold, and when large values of the spin flip rate are considered.

3.4 Fluctuation of the Polarization Angles

In order to study polarization fluctuations, it is convenient to express the electric field in terms of the polarization orientation ϕ and ellipticity χ angles

$$\begin{aligned} \vec{E} &= \sqrt{P} [(\cos \chi \cos \phi - i \sin \chi \sin \phi) \hat{x} \\ &+ (\cos \chi \sin \phi + i \sin \chi \cos \phi) \hat{y}] e^{i(\omega t + \varphi_0)}, \end{aligned} \quad (3.13)$$

or alternatively in the circular representation⁶

$$\vec{E} = \sqrt{\frac{P}{2}} [(\cos \chi + \sin \chi) e^{-i\phi} \hat{e}_+ + (\cos \chi - \sin \chi) e^{i\phi} \hat{e}_-] e^{i(\omega t + \varphi_0)}, \quad (3.14)$$

⁶The unitary circular vectors read $\hat{e}_\pm = \frac{1}{\sqrt{2}}(\hat{x} \mp i\hat{y})$.

P being the total power and φ_0 an arbitrary phase. The meaning of these two angles is more explicit by introducing the Stokes parameters S_j defined by the following relationships

$$S_0 = |E_+|^2 + |E_-|^2 = |E_x|^2 + |E_y|^2 = P, \quad (3.15a)$$

$$S_1 = 2\text{Re}(E_+E_-^*) = |E_x|^2 - |E_y|^2 = P \cos(2\phi) \cos(2\chi), \quad (3.15b)$$

$$S_2 = -2\text{Im}(E_+E_-^*) = -2\text{Re}(E_x^*E_y) = P \sin(2\phi) \cos(2\chi), \quad (3.15c)$$

$$S_3 = |E_+|^2 - |E_-|^2 = -2\text{Im}(E_x^*E_y) = P \sin(2\chi). \quad (3.15d)$$

Hence S_j/S_0 for $j = 1, 2, 3$ describes the Cartesian components of a unit sphere. The spherical coordinates are the polarization angle $2\phi \in [0, 2\pi]$ and the ellipticity angle $2\chi \in [-\pi/2, \pi/2]$. The polarized light is such that the relation $S_0^2 = S_1^2 + S_2^2 + S_3^2$ is fulfilled at any time.

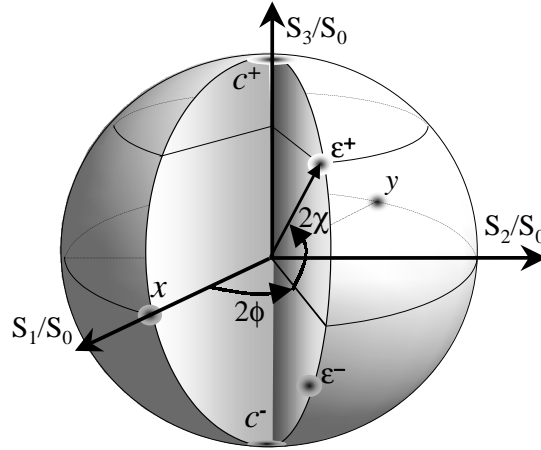


Figure 3.8: Poincaré sphere: $x(y)$ -LP state along the $\hat{x}(\hat{y})$ direction; c^\pm are right and left circularly polarized states, ϵ^\pm are right and left elliptically polarized states. Shaded circles represent fluctuations around these states.

In the steady state, $\phi = 0(\phi = \pi/2)$ for a x -LP (y -LP) and $\chi = 0$. Fluctuations of the polarization angles around LP states are obtained by linearizing Eq. (3.14). We find that

$$\delta\chi = \frac{R + R^*}{4Q}, \quad \delta\phi = i\frac{R - R^*}{4Q}, \quad (3.16)$$

where R and R^* were defined in Sec. 2.4. Equation (3.16) reveals the connection between the ellipticity fluctuations and the notation used in this work in terms of power fluctuations of the circular components. Hence, fluctuations of the circular components are linked to movements orthogonal to the equatorial plane of the Poincaré sphere.

The fluctuations in $\delta\phi$ and $\delta\chi$ are governed by

$$\begin{pmatrix} \dot{\delta\phi} \\ \dot{\delta\chi} \\ \dot{\delta} \end{pmatrix} = \begin{pmatrix} \pm 2\gamma_a & \mp 2\gamma_p & -\alpha\kappa \\ \pm 2\gamma_p & \pm 2\gamma_a & \kappa \\ 0 & -4\gamma D_0 Q^2 & -(\gamma_s + 2\gamma Q^2) \end{pmatrix} \begin{pmatrix} \delta\phi \\ \delta\chi \\ \delta \end{pmatrix} + \begin{pmatrix} F_\phi \\ F_\chi \\ F_\delta \end{pmatrix}, \quad (3.17)$$

which is directly obtained from Eqs. (2.33) and (3.16). The real Langevin terms obey

$$\begin{aligned} \langle F_\phi(t)F_\phi(t') \rangle &= \langle F_\chi(t)F_\chi(t') \rangle = \frac{\gamma\beta_{sp}D_0}{2Q^2}\delta(t-t'), \\ \langle F_\delta(t)F_\delta(t') \rangle &= \left(\frac{\gamma}{\kappa}\right)^2 2\beta_{sp}D_0Q^2, \\ \langle F_\chi(t)F_\delta(t') \rangle &= \frac{\gamma^2\beta_{sp}D_0}{\kappa}\delta(t-t'), \\ \langle F_\phi(t)F_\chi(t') \rangle &= \langle F_\phi(t)F_\delta(t') \rangle = \langle F_\phi(t)F_\chi(t') \rangle = 0. \end{aligned} \quad (3.18)$$

Equation (3.17) is the starting point of other works that invoking the limit of large γ_s , i.e. $\dot{\delta} \approx 0$, the dimensionality is reduced to two. In this limit, the fluctuations of δ are slaved to the fluctuations of $\delta\chi$

$$\delta(t) \approx \frac{-4\gamma D_0 Q^2}{\gamma_s + 2\gamma Q^2} \delta\chi(t) + \frac{F_\delta(t)}{\gamma_s + 2\gamma Q^2}.$$

It is worth noting that such an approximation is only justified well within the COs region. In spite of generality, we maintain the dynamics of $\delta(t)$, which allows us to analyze fluctuations for any value of γ_s and to extend the investigation of polarization fluctuations into the PROs region.

The spectral density of the polarization fluctuations is obtained by solving the linear system of Eq. (3.17) in the Fourier domain. The result is

$$S_\Xi(\omega) = \frac{\gamma\beta_{sp}D_0}{2Q^2} \left[\frac{\mathcal{A}_\Xi(\omega) + \mathcal{B}_\Xi(\omega)}{\mathcal{C}(\omega)} \right] \quad (3.19)$$

where $\Xi = \phi, \chi, \delta$ and $\mathcal{A}, \mathcal{B}, \mathcal{C}$ are polynomial functions of ω defined in the Appendix A.

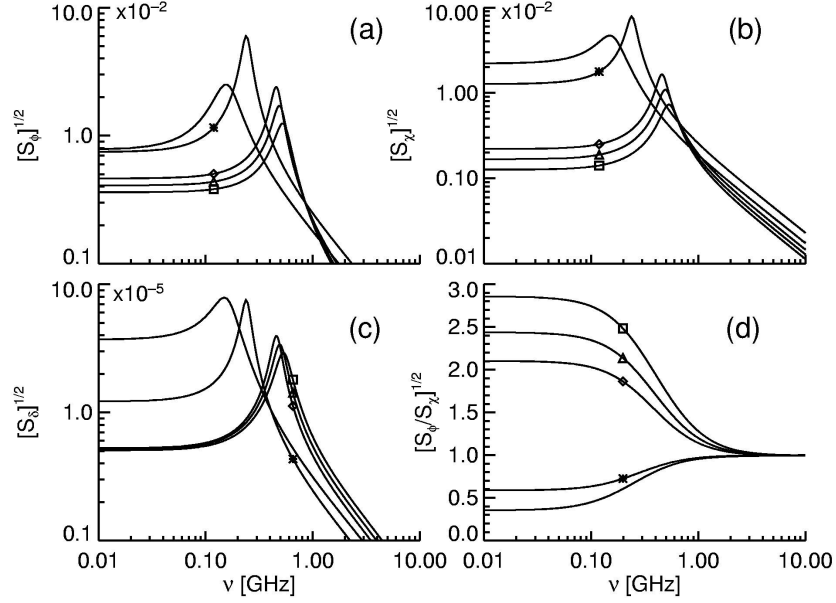


Figure 3.9: Power spectra (in arbitrary units) of the polarization fluctuations, (a) $S_\phi(\omega)$, (b) $S_\chi(\omega)$, (c) $S_\delta(\omega)$ and (d) the ratio $S_\phi(\omega)/S_\chi(\omega)$. The same parameters as in Fig. 3.6(a,b), corresponding to a COs region and when crossing a PS. Meaning of the symbols: (*) $\mu = 1.047$, (no symbol) $\mu = 1.083$, (\diamond) $\mu = 1.120$, (\triangle) $\mu = 1.15$, (\square) $\mu = 1.20$. The LF solution is considered below PS while the HF solution is the only stable above the PS.

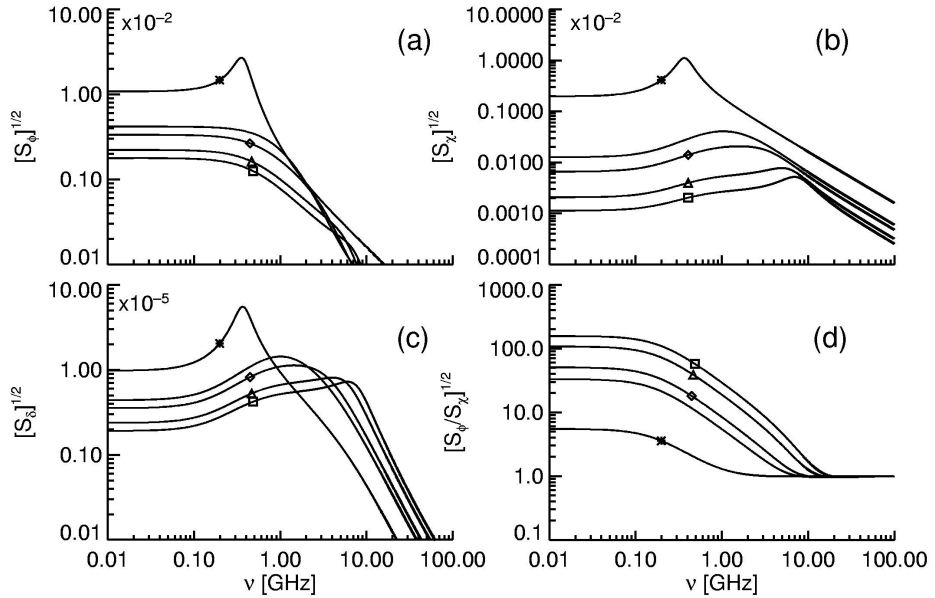


Figure 3.10: Power spectra (in arbitrary units) of the polarization fluctuations, (a) $S_\phi(\omega)$, (b) $S_\chi(\omega)$, (c) $S_\delta(\omega)$ and (d) the ratio $S_\phi(\omega)/S_\chi(\omega)$. The parameters correspond to the situation described in Fig. 3.2(b), taking $\gamma_s/\gamma = 40$. The HF solution is considered for different currents: (*) $\mu = 1.1$, (no symbol) $\mu = 1.72$, (\diamond) $\mu = 2.12$, (\triangle) $\mu = 3.56$, (\square) $\mu = 5.00$.

Some other interesting relationships can be obtained by the linearization

of Eqs. (3.15a)-(3.15d)

$$S_q(\omega) = 4(2Q^2)^2 S_\chi(\omega), \quad (3.20a)$$

$$S_+(\omega) = S_-(\omega) = \frac{1}{4} S_P(\omega) + (2Q^2)^2 S_\chi(\omega), \quad (3.20b)$$

$$\begin{aligned} M &\equiv \left\langle \frac{P_{nl}}{P_l} \right\rangle \approx \langle |\delta\phi(t)|^2 \rangle + \langle |\delta\chi(t)|^2 \rangle = \\ &= \frac{1}{2\pi} \int_{-\infty}^{\infty} [S_\phi(\omega) + S_\chi(\omega)] d\omega. \end{aligned} \quad (3.20c)$$

First, we consider a situation where a PS takes place within a region of COs. The power spectra of the polarization fluctuations, $S_\phi(\omega)$, $S_\chi(\omega)$, $S_\delta(\omega)$ in Fig. 3.9, display a single peak at the COs frequency Ω_P . Note that the peak at Ω_R is absent in all the cases, since these variables only describe polarization fluctuations onto the Poincaré sphere. When increasing the current from threshold to PS, the LF solution lases and the frequency Ω_P decreases while the effective dichroism increases reflecting itself in broad peaks in the power spectra. Below the PS, the fluctuations in the ellipticity angle are considerably larger than in the polarization orientation, being reflected in the ratio $S_\phi(\omega)/S_\chi(\omega)$ shown in Fig. 3.9(d). Once the PS takes place, the HF solution starts to lase and the frequency Ω_P increases linearly when increasing the current level. We also note that in this situation, the peaks are much narrower and that the polarization fluctuations prefer the polarization orientation angle. In a second instance, the Fig. 3.10 illustrates the behavior of the polarization fluctuations in the limit of small linear anisotropies. No PS occurs in this case and the VCSEL always emits in the HF solution. Close-to-threshold there exists a narrow region of COs that leads to a similar behavior to that already mentioned in Fig. 3.9. For higher injection levels a region of PROs appears, where the fluctuations in the polarization angle ϕ decouple and experience damped relaxation without oscillation. Consequently, the power spectra of $S_\phi(\omega)$ does not display any peak, while $S_\chi(\omega)$, $S_\delta(\omega)$ have a peak at the PROs frequency, rather broad due to the relatively large effective dichroism. It is worth remarking that the fluctuations in polarization orientation are large because of the weak birefringence.

3.5 Role of the Spin Flip and Birefringence

Since our theoretical description is valid for arbitrary values of the birefringence and spin flip, in this section we give a complete description of the role of these parameters. We look at the power spectra while the polarization state is followed on the Poincaré sphere.

Power spectra for small and large values of γ_s , in the absence of birefringence, are shown in Fig. 3.11. As expected, the CO peak is absent in the

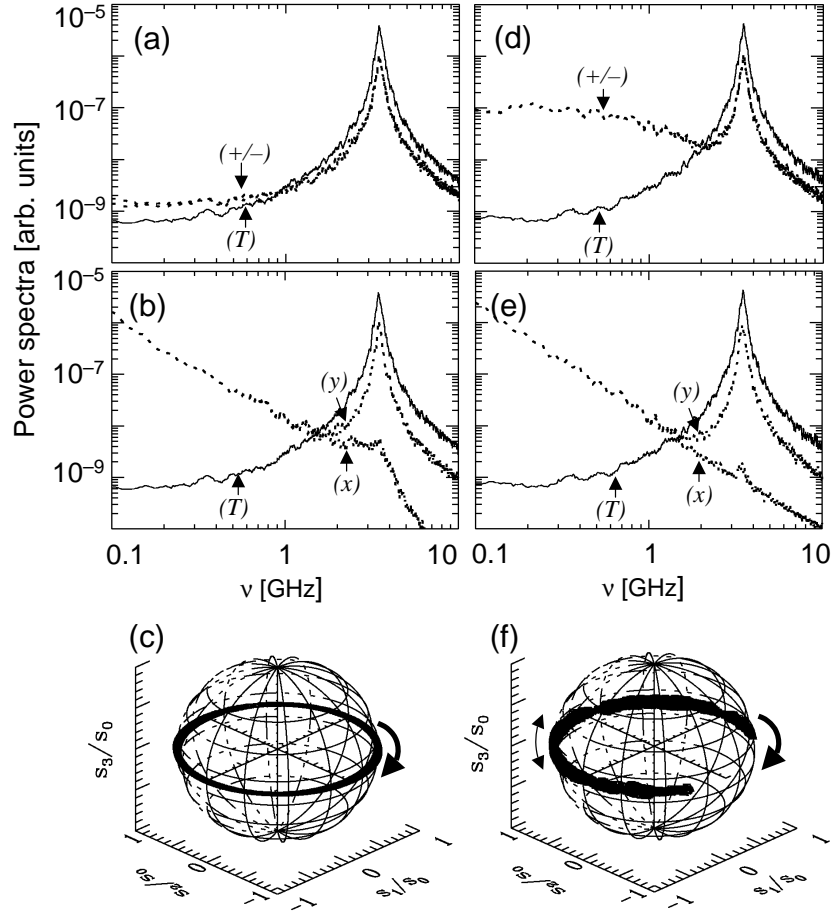


Figure 3.11: Study of the effect of γ_s in the absence of birefringence, in the power spectra of the circular (a,d) and linear components (b,e). Evolution of the polarization state on the Poincaré sphere (c,f) for small values of the spin flip rate $\gamma_s = 10 \text{ ns}^{-1}$ in (a,c), $\gamma_s = 100 \text{ ns}^{-1}$ in (d,f). The normalized current is $\mu = 1.8$. The meaning of the symbols is: (T) = S_P , (+/-) = S_{\pm} , (x) = S_x and (y) = S_y .

power spectra of the circular components [See Fig. 3.11(a,d)]. The main difference between the two cases appears at low frequency: while P_{\pm} have large anticorrelation for large γ_s , this anticorrelation is reduced for small γ_s . This effect can be understood as follows: for slow spin flip rates each of the two circular components burns carriers from its own reservoir N_{\pm} separately. In this case there is no competition and therefore small anticorrelated fluctuations are observed in Fig. 3.11(a). On the other hand, for fast spin flip rates, the two circular components have to share almost the same carrier reservoir since $N_+ \approx N_-$. The latter causes strong anticorrelation because of PPN [Fig. 3.11(d)]. The power spectra of the two linear components are similar for small and large values of γ_s [Fig. 3.11(b,e)]. They show pronounced anticorrelations at low frequencies linked to important fluctuations of the polarization orientation. Both lasing and nonlasing power spectra display a peak at the relaxation

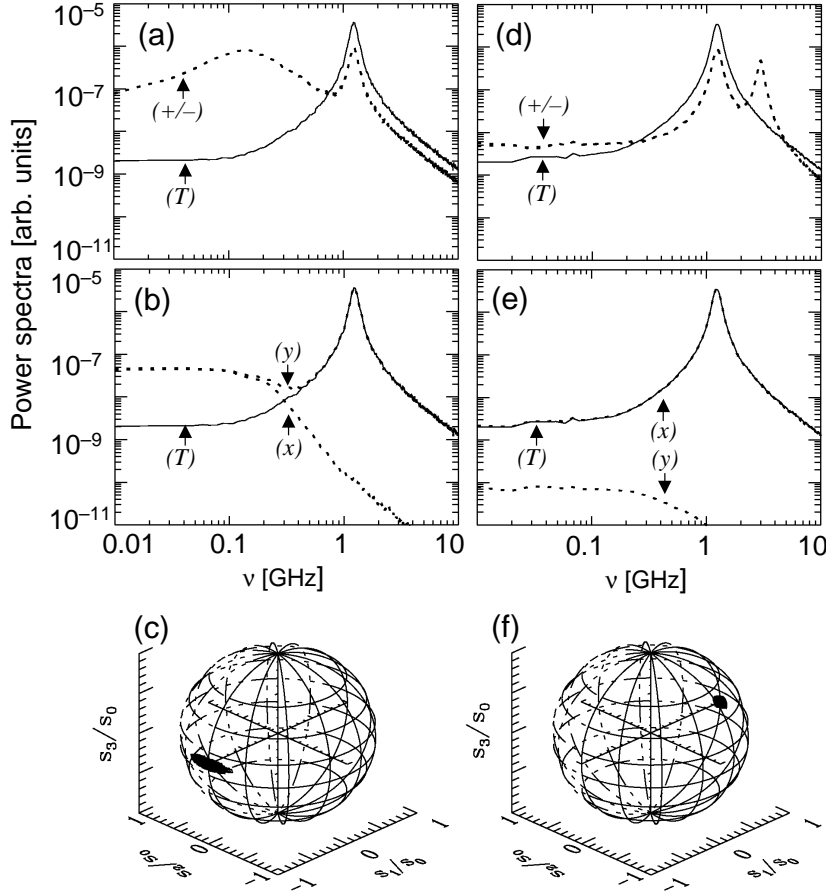


Figure 3.12: Study of the effect of γ_p on power spectra of the circular (a,d) and linear (b,e) components when $\gamma_s = 50 \text{ ns}^{-1}$. Evolution on the Poincaré sphere for small birefringence $\gamma_p = 0.1 \text{ ns}^{-1}$ (a,c) and $\gamma_p = 10 \text{ ns}^{-1}$ (d,f). The normalized current is $\mu = 1.1$. The meaning of the symbols is the same as in Fig. 3.11.

oscillation frequency.

The role of the birefringence is shown in Fig. 3.12 for a fixed value of the spin flip rate. For small birefringence, $\gamma_p = 0.1 \text{ ns}^{-1}$, we observe large anticorrelation of circular and linear components at low frequencies [Fig. 3.12(a,b)]. This fact indicates important polarization fluctuations. The main role of the birefringence is to fix a polarization orientation, reducing consequently the polarization fluctuations. For a larger birefringence, $\gamma_p = 10 \text{ ns}^{-1}$, we observe that the anticorrelation of the circular components has been considerably reduced [Fig. 3.12(d)] being negligible for the linear components [Fig. 3.12(e)]. We note that a PS occurs when the birefringence is increased and the fluctuations on the Poincaré sphere move to the opposite direction on the equator of the sphere. In addition, the CO peak appears at larger frequency than the RO peak.

It is also illustrative to analyze the evolution of the polarization state on the Poincaré sphere [Fig. 3.8]. We observe that for small γ_p the fluctuations

prefer the equatorial direction [Fig. 3.12(c)]. In the limiting case of $\gamma_p=0$, there is a zero eigenvalue of Eq. (2.34) associated with the arbitrariness of the polarization orientation, and the polarization diffuses along LP states with different orientation angles due to the presence of noise. The polarization evolves along the equator of the sphere with small ellipticity fluctuations controlled by γ_s [Fig. 3.11(c,f)]. When γ_s is large, the two remaining eigenvalues become real. One of them approaches to zero when $\gamma_s \rightarrow \infty$, describing diffusion of the ellipticity angle. In the latter, there is no preference for any polarization state and the fluctuations cover the whole surface of the Poincaré sphere [60]. When $\gamma_p \neq 0$, the eigenvalue that describes the diffusion of the polarization orientation angle becomes nonzero, providing the stability of the steady state. For moderate to large values of γ_p , we observe that the polarization orientation is fixed and the fluctuations on the Poincaré sphere have a rather circular shape [Fig. 3.12(f)].

3.6 Polarization Anticorrelations

To better characterize the correlations among two orthogonal components we compute the normalized crosspower spectral density [50] which reads

$$C_{AB}(\omega) = \frac{S_{A+B}(\omega) - S_A(\omega) - S_B(\omega)}{2\sqrt{S_A(\omega)S_B(\omega)}}, \quad (3.21)$$

where $A(t)$ and $B(t)$ are two given signals, while S_A and S_B represent their respective power spectra. $C_{AB}(\omega) = 1$ (-1) corresponds to perfect correlation (anticorrelation) in the fluctuations of the two signals. The normalized crosspower spectral density between the power fluctuations of the two circular components δP_+ and δP_- can be obtained from

$$\begin{aligned} C_{+-}(\omega) &= \frac{S_P(\omega) - S_q(\omega)}{S_P(\omega) + S_q(\omega)} \\ &= \frac{\text{Re} \int_{-\infty}^{\infty} \langle \delta \tilde{P}_+(\omega) \delta \tilde{P}_-^*(\omega') \rangle d\omega'}{\int_{-\infty}^{\infty} \langle \delta \tilde{P}_{\pm}(\omega) \delta \tilde{P}_{\pm}^*(\omega') \rangle d\omega'}. \end{aligned} \quad (3.22)$$

On replacing the expression for $S_P(\omega)$ and $S_q(\omega)$ from Eqs. (3.9a) and (3.9b) into Eq. (3.22) we obtain the exact expression for C_{+-} . This expression can be simplified at low frequencies in the case of close to perfect anticorrelation, i.e., $C_{+-}(\omega \approx 0) \approx -1$, to

$$C_{+-}(\omega = 0) \approx -1 + \frac{1}{2Q^4} \frac{[\frac{\gamma_p}{\kappa} \Gamma - \varepsilon \alpha]^2}{[\alpha^2 + \Gamma^2]}, \quad (3.23)$$

with $\Gamma \equiv \frac{\gamma_s}{2\gamma Q^2}$. It is easy to see from Eq. (3.22) that the fluctuations are correlated at the frequency where $S_P(\omega) \gg S_q(\omega)$, close to Ω_R , and the fluctuations

are anticorrelated when $S_P(\omega) \ll S_q(\omega)$, near the CO peak Ω_P . We can interpret these two limits with the help of the Poincaré sphere. The fluctuations of the total number of photons are linked to movements toward the inside and outside of the Poincaré sphere surface [Fig. 3.8]. These movements are equivalent for all the points on the sphere, and therefore provide correlation between circular components. Anticorrelations between components are associated with movements on the Poincaré sphere, i.e., polarization orientation and ellipticity fluctuations.

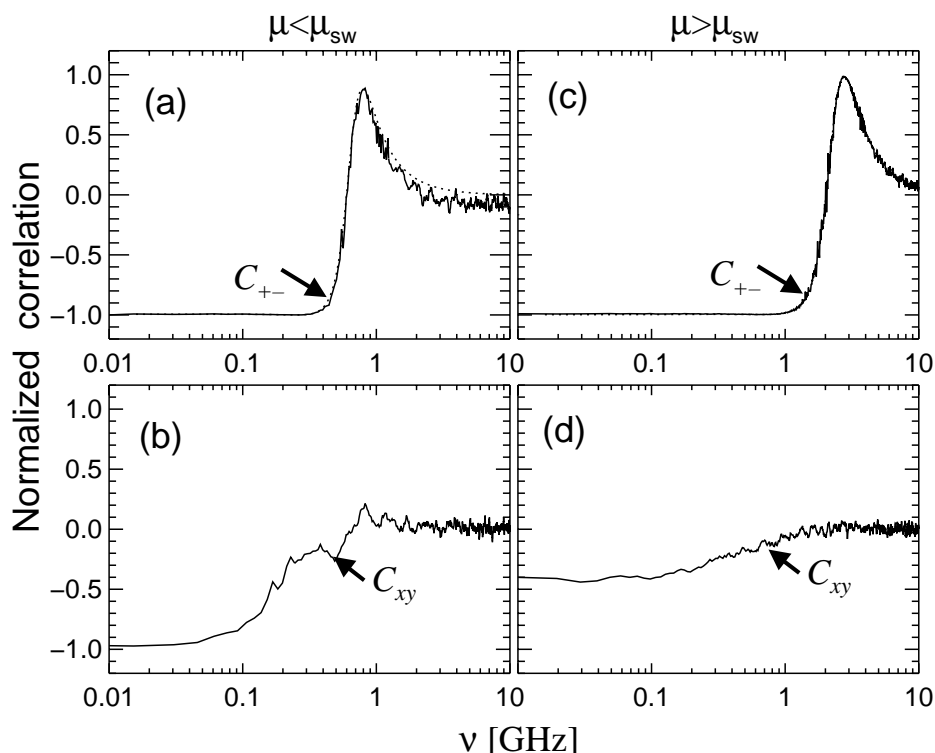


Figure 3.13: Normalized crosscorrelation of the circular components C_{+-} (a,c) and of the linear components C_{xy} (b,d) corresponding to the same situation as in Fig. 3.6. Dotted lines in (a,c) represent theoretical prediction given by Eq. (3.22).

In Fig. 3.13 we show the results for the normalized crosscorrelation function, Eq. (3.22), under the same conditions as in Fig. 3.6. In the circular basis C_{+-} , we find close to perfect anticorrelations for low frequencies, and strongly correlated fluctuations ($C_{+-} \approx 1$) for frequencies close to the RO peak. In the linear basis, C_{xy} displays partially anticorrelated fluctuations at low frequency ($\nu \leq 1$ GHz) due to PPN [31, 61] above the PS, and large anticorrelation below the PS which corresponds to the two LP states being stable. The lack of anticorrelation above PS might be attributed to the modification of the effective birefringence due to the nonlinearities when the injection current is increased. Below the PS, the effective birefringence Ω_P/π , reaches a minimum. This fact leads to preferential fluctuations of the polarization

orientation, and consequently anticorrelated fluctuations of the linear components. On the contrary, above the PS, the effective birefringence gradually increases with increasing distance from the PS leading to a reduction of the anticorrelation.

Chapter 4

Summary, Discussion and Perspectives

THE polarization field vector of vertical-cavity surface-emitting lasers (VCSELs) has been investigated within a model that focuses in the allowed optical transitions among the magnetic sub-levels of the conduction and valence bands of a semiconductor, namely, the Spin Flip Model (SFM) introduced by San Miguel-Feng-Moloney in 1995. We put forward the governing equations that apply for single longitudinal VCSELs operating in the fundamental transverse mode. We derived, from quantum mechanical requirements, the semiclassical Langevin noise sources that arise from spontaneous emission processes. The linearization of the SFM, when considering fluctuations around stationary linearly polarized solutions, was introduced as the starting point for a later investigation of intensity and polarization fluctuations. We concentrated our discussion in those physical parameters that may be relevant in the polarization mode selection and in the determination of polarization fluctuations.

In chapter 3, we presented analytical and numerical investigations of the polarization resolved power spectra of linearly polarized states based on a semiclassical framework valid for arbitrary values of the spin flip rate and birefringence. It constitutes a generalization of previous studies where the adiabatic elimination of the spin dynamics was taken. A proper classification of the regimes of operation in terms of the eigenvalues and eigenvectors of the linearized systems has been useful for the subsequent formulation and interpretation of the polarization fluctuations. Two qualitative different regimes of operation were observed, namely polarization relaxation oscillations of the ellipticity angle and carrier difference (PROs), and coupled oscillations of the polarization angles (COs). Most of the reported results apply to VCSELs operating the COs regime but the access to the PROs is just a matter of parameters, basically current level and spin flip rate. We presented specific results for the power spectra of linearly polarized states when the VCSEL was driven across a nonthermal polarization switching. The power spectrum of the total

intensity fluctuations displays a peak at the relaxation oscillation frequency. In the regime of coupled oscillations, the power spectra of the two circular components coincide and show an additional peak associated with the effective birefringence splitting. When analyzing the evolution of the polarization state on the Poincaré sphere, we were able to separate the effects of the birefringence and the spin flip rate. In the absence of birefringence, the spin flip rate controls the ellipticity fluctuations that are related to the fluctuations of the circular components. On the other hand, for a fixed spin flip rate the birefringence controls the polarization orientation fluctuations. The frequency dependence of the normalized cross-correlation function for both linear and circular components was also presented. In particular, we found that the two circular components are strongly anticorrelated at low frequencies while they display a nearly perfect correlation close to the relaxation oscillation peak. The linear components (lasing and nonlasing) present a nonvanishing crosscorrelation function at low frequencies. Linear components display partially anticorrelated fluctuations below the polarization switching which correspond to the two linearly polarized states being stable. Above the polarization switching, the anticorrelation nearly vanishes being attributed to an abrupt increase of the effective birefringence that reduce the magnitude of the polarization fluctuations. Further investigations of the polarization resolved power spectra of elliptical and dynamical states, where the total intensity and polarization fluctuations do not decouple, should provide a more complete understanding of the noise properties of vertical-cavity surface-emitting lasers.

Although our semiclassical analysis of fluctuations is consistent with quantum noise sources, there are several aspects that become important when establishing the limits to achieve quantum noise levels, such as the standard quantum limit and quantum squeezing. They include shot noise in the carrier recombination, statistics of the pump fluctuation and interference of the vacuum field entering in to the VCSEL cavity (input-output formalism [9]). Notwithstanding, the semiclassical approach have led to valuable theoretical predictions that successfully compares with the experiments, namely: polarization switching from the low frequency to the high frequency mode of nonthermal origin, existence of anticorrelated fluctuations between the polarization components, interpretation of the characteristic frequencies in the power spectra, nonlinear anisotropies, etc. Hence, our study should establish the elementary concepts for further investigation based on sophisticated fully quantum-mechanical models.

Outlook

There exist however several hypothesis when deriving the SFM rate equations, some of them already commented, that fix the limits of applicability. Some of the more restrictive include: flat gain spectrum, unrealistic α -factor, absence of transverse and thermal effects. It is possible to account for some

of these effects by extending the SFM to a model for the VCSEL dynamics proposed by S. Balle in 1999 [62]. This model allows to include: a realistic gain and refractive index spectra, a realistic α -factor, transverse and thermal effects. Some results based on the analysis of the extended SFM have been presented [63, 64] and it is currently being matter of research.

Hypothesis when deriving the Spin Flip Model

- *Flat gain spectrum:* When replacing the band structure of the semiconductor material by a four-level system, we lose the contribution of the possible optical transitions at electron wavevectors $k_{\perp} \neq 0$. As a consequence the gain spectrum that results has a Lorentzian shape –typical of an atomic system–. This spectrum becomes flat when invoking the limit of large γ_{\perp} , and the material polarization is adiabatically eliminated.
- *α -factor:* The α -factor in a two-level system has to be artificially introduced as the normalized frequency detuning with respect to the gain peak. Operation on the blue side of the gain spectrum ($\Omega > \omega_g$) lead to negative values for the α -factor and to carrier-guiding, being in contradiction with the basic properties of sc lasers. The α -factor in a quantum well semiconductor laser is not a constant, but in general, a function of the frequency and the carrier inversion.
- *Transverse effects:* The standard SFM assumes fundamental transverse mode operation. However, it is commonly observed that higher-order transverse modes start to appear when the VCSEL is driven far from the threshold current. Transverse effects inherently occur in a quite broad frequency-band and involving inhomogeneous carrier distributions; thus it is imperative to incorporate a correct description of the gain and α -factor spectra.
- *Thermal effects:* The SFM assumes constant active region operation, however two thermal effects appear when the injection current increases. First, when the current flows through the VCSEL structure, predominantly heats the spatial zone close to the cavity axis, which leads to an inhomogeneous temperature distribution across the lateral direction. This effect provides a lateral waveguide that focuses the optical field. And second, the cavity modes and gain curve redshifts due to the temperature dependence of the materials composing the VCSEL.

Improvements of the Spin Flip Model

- Realistic gain and refractive index spectra of QWs, including a correct frequency and carrier inversion dependence. Since different modes, both polarization and transverse modes, operate at different frequency, this

contribution lead to different modal gains and refractive index for each of them.

- Realistic α – *factor* for the quantum well, being a function of the frequency and carrier inversion. In addition, the material is intrinsically carrier-antiguinding, i.e., the index of refraction decreases when the carrier density increases. Despite other guiding mechanisms, this effect provides self-defocusing of the electric field.
- Thermal effects can be easily included through the thermal lensing and thermal shift effects. Within this model, it has been demonstrated that thermal mechanisms of polarization switching and that coming from phase instabilities, explained by the SFM, can coexist depending on the VCSEL characteristics [29].
- Transverse and polarization dynamics are described in an unified way, by including electric field diffraction and carrier diffusion.

Acknowledgments

I wish to specially thank Professors M. San Miguel and C. R. Mirasso for their advice and encouragement on this work; to S. Balle, A. Scirè, L. Pesquera, A. Valle, I. Maurin, W. Elsässer and C. Degen, among others, for their constructive criticisms and ideas that contributed to improve the scientific quality of this report.

Although money does not always bring one happiness, I wish also thank to Ministerio de Educación y Cultura for funding through the fellowship AP98-78215109. The presentation of this work in several international conferences [see curriculum] have been possible from the financial support received from different projects. We thank to the European Commission through the VISTA HP-TRN network and the Ministerio de Ciencia y Tecnología under projects TIC99-0645-C05-02 and BFM2000-1108.

Appendix A

Definitions

The following functions define the power spectra of the polarization components as was described in Sec. 3.4,

$$\begin{aligned} \mathcal{C}(\omega) &\equiv \mathcal{D}(i\omega)\mathcal{D}(-i\omega) = \\ &= [(\Gamma_s \mp 2\varepsilon_a)\omega^2 - \{(\varepsilon_a^2 + \varepsilon_p^2)\Gamma_s \mp b(\varepsilon_a + \alpha\varepsilon_p)\}]^2 \\ &+ \omega^2 [\omega^2 - \{\varepsilon_a^2 + \varepsilon_p^2 + b \mp 2\varepsilon_a\Gamma_s\}]^2. \end{aligned} \quad (\text{A.1})$$

$$\begin{aligned} \mathcal{A}_\phi(\omega) &= [\omega^2 - b \pm \varepsilon_a\Gamma_s]^2 + \omega^2 [\Gamma_s \mp \varepsilon_a]^2, \\ \mathcal{B}_\phi(\omega) &= \omega^2(\alpha c \mp \varepsilon_p)^2 + [\alpha b \mp \varepsilon_p\Gamma_s \pm c(\varepsilon_p - \alpha\varepsilon_a)]^2. \end{aligned} \quad (\text{A.2})$$

$$\begin{aligned} \mathcal{A}_\chi(\omega) &= \varepsilon_p^2(\omega^2 + \Gamma_s^2), \\ \mathcal{B}_\chi(\omega) &= \omega^2(\gamma_s \mp \varepsilon_a)^2 + (\omega^2 \pm \gamma_s\varepsilon_a \mp \alpha c\varepsilon_p)^2. \end{aligned} \quad (\text{A.3})$$

$$\begin{aligned} \mathcal{A}_\delta(\omega) &= (\varepsilon_p b)^2 / \kappa^2, \\ \mathcal{B}_\delta(\omega) &= [\{c(\varepsilon_a^2 + \varepsilon_p^2 - \omega^2) \mp b\varepsilon_a\}^2 + \omega^2(b \mp 2c\varepsilon_a)^2] / \kappa^2. \end{aligned} \quad (\text{A.4})$$

In order to simplify the notation, we have defined these new quantities

$$\varepsilon_{a,p} \equiv 2\gamma_{a,p}, \quad \Gamma_s \equiv \gamma_s + 2\gamma Q^2, \quad b \equiv 4\kappa\gamma D_0 Q^2, \quad c \equiv 2\gamma Q^2.$$

In Chapter 3, we defined the power spectra of polarization fluctuations through

$$S_\Xi(\omega) = \frac{\gamma\beta_{sp}D_0}{2Q^2} \left[\frac{\mathcal{A}_\Xi(\omega) + \mathcal{B}_\Xi(\omega)}{\mathcal{C}(\omega)} \right] \quad (\text{A.5})$$

where $\Xi = \phi, \chi, \delta$. The asymptotic behavior of the power spectra in the limit of large frequencies is

$$S_\phi(\omega) = S_\chi(\omega) = \left(\frac{\kappa}{c}\right)^2 S_\delta(\omega) \xrightarrow{\omega \rightarrow \infty} \frac{1}{1 + \left(\frac{\omega}{\Delta\omega}\right)^2}, \quad (\text{A.6})$$

that behaves like the spectra of an Ornstein-Uhlenbeck process [Eq. (2.12)] with correlation time

$$\tau^{-1} \equiv \Delta\omega = \sqrt{\Gamma_s^2 + 2(\varepsilon_a^2 - \varepsilon_p^2 - b)}.$$

Another interesting aspect is to analyze the shape of the fluctuations onto the Poincaré plane $\phi - \chi$. At low frequencies we find that

$$\begin{aligned} \left| \frac{S_\phi}{S_\chi} \right|_{\omega=0} &\approx \frac{b^2 + [\alpha b \mp \varepsilon_p \gamma_s]^2}{\varepsilon_p^2 [\Gamma_s^2 + \alpha^2 c^2]} \\ &\xrightarrow{\varepsilon_p \rightarrow 0} (1 + \alpha^2) \frac{b^2}{\varepsilon_p^2 \Gamma_s^2} \gg 1 \\ &\xrightarrow{\mu \rightarrow D_0} 1. \end{aligned}$$

Fluctuations display a circular shape in the $\phi - \chi$ plane close-to-threshold, while they preferably follow the ϕ -direction for small birefringence.

Appendix B

Itô Transformation

Let us concentrate in Eq. (2.24a) for the complex slowly-varying amplitude of the electric field

$$dE_{\pm} = \{ \kappa(1 + i\alpha)[D \pm d - 1]E_{\pm} - (\gamma_a + i\gamma_p)E_{\mp} \} dt + \sqrt{\beta_{sp}\gamma(D \pm d)} dW_{\pm}(t), \quad (\text{B.1})$$

where we have introduced the complex Wiener process as $dW_{\pm} \equiv \xi_{\pm}(t)dt$. We are interested to know which stochastic equations verify the amplitudes and phases of the electric field, $P_{\pm}(t)$ and $\phi_{\pm}(t)$, with $E_{\pm}(t) = \sqrt{P_{\pm}(t)}e^{i\phi_{\pm}(t)}$. For these purposes, we introduce an auxiliary variable $\rho_{\pm} = \frac{1}{2} \ln P_{\pm}$, then

$$d(\rho_{\pm} + i\phi_{\pm}) = d(\ln E_{\pm}) = \ln(E_{\pm} + dE_{\pm}) - \ln(E_{\pm}).$$

We expand the right hand of the above equation at first order in dt . Making use of the Itô rules for a generic real Wiener process $dW_a(t)$ [11, 12], are that $dW_a(t)^2 = dt$ and $dW_a(t)^{2+N} = 0$ for $N > 0$, we arrive to

$$d\rho_{\pm} = \kappa(D \pm d - 1)dt - (\gamma_a \cos \phi \pm \gamma_p \sin \phi) \sqrt{\frac{P_{\mp}}{P_{\pm}}} dt + \sqrt{\frac{\gamma\beta_{sp}(D \pm d)}{P_{\pm}}} dW_{P_{\pm}} - \frac{1}{2} \frac{\gamma\beta_{sp}(D \pm d)}{E_{\pm}^2} [dW_{R,\pm} + i dW_{I,\pm}]^2, \quad (\text{B.2a})$$

$$d\phi_{\pm} = \alpha\kappa(D \pm d - 1)dt - (\gamma_p \cos \phi \mp \gamma_a \sin \phi) \sqrt{\frac{P_{\mp}}{P_{\pm}}} dt + \sqrt{\frac{\gamma\beta_{sp}(D \pm d)}{P_{\pm}}} dW_{\phi_{\pm}}, \quad (\text{B.2b})$$

with $\phi = \phi_+ - \phi_-$. It is worth noting that since $dW_{R,\pm}, dW_{I,\pm}$, representing the real and imaginary parts of dW_{\pm} , are independent, then the last term

of Eq. (B.2a) vanishes. The second remark is the also the Wiener processes $dW_{P_{\pm}}, dW_{\phi_{\pm}}$ are independent, being defined through the orthogonal transformation

$$dW_{P_{\pm}}(t) = \cos \phi_{\pm} dW_{R,\pm}(t) + \sin \phi_{\pm} dW_{I,\pm}(t), \quad (\text{B.3a})$$

$$dW_{\phi_{\pm}}(t) = -\sin \phi_{\pm} dW_{R,\pm}(t) + \cos \phi_{\pm} dW_{I,\pm}(t). \quad (\text{B.3b})$$

As a final step, we apply the Itô rules to the variable ρ_{\pm}

$$dP_{\pm} = d[e^{2\rho_{\pm}}] = e^{2(\rho_{\pm}+d\rho_{\pm})} - e^{2\rho_{\pm}} = 2P_{\pm} (d\rho_{\pm} + d\rho_{\pm}^2 + \dots).$$

Introducing Eq. (B.2a) in to this last expression, we arrive to

$$\begin{aligned} dP_{\pm} = & 2\kappa(D \pm d - 1)P_{\pm}dt - 2(\gamma_a \cos \phi \pm \gamma_p \sin \phi) \sqrt{P_+ P_-} dt \\ & + 2\gamma\beta_{sp}(D \pm d) dt + \sqrt{4\gamma\beta_{sp}(D \pm d)} P_{\pm} dW_{P_{\pm}}, \end{aligned} \quad (\text{B.4})$$

that is nothing else that Eq. (3.6a). The interesting result, from this stochastic transformation, is the term $2\gamma\beta_{sp}(D \pm d)$ in Eq. (B.4), that accounts for the mean value of spontaneously emitted photons in each circular polarization. The remaining equations in Sec. 3.3 can be straightforwardly derived, by defining $\xi_{P_{\pm}} = dW_{P_{\pm}}/dt$ and $\xi_{\phi_{\pm}} = dW_{\phi_{\pm}}/dt$.

Bibliography

- [1] A. L. Schawlow and C. H. Townes, “Infrared and optical masers,” *Phys. Rev.*, vol. 112, p. 1940, 1958.
- [2] T. H. Maiman, “Stimulated optical radiation in ruby,” *Nature*, vol. 187, p. 493, 1960. See also in Ref. [7], Chapter 5.
- [3] R. N. Hall, G. E. Fenner, J. D. Kingsley, T. J. Soltys, and R. O. Carlson, “Coherent light emission from GaAs junctions,” *Phys. Rev. Lett.*, vol. 9, p. 366, 1962.
- [4] G. P. Agrawal, *Long-wavelength semiconductor lasers*. N. Y.: Van Nostrand Reinhold, 1986.
- [5] W. Nakwaski and M. Osinski, “Thermal properties of vertical-cavity surface-emitting lasers,” *Progress in Optics XXXVIII*, pp. 165–262, Amsterdam: Elsevier North-Holland, 1998.
- [6] K. Iga and F. Koyama, “Surface-emitting lasers,” *Semiconductor lasers II. Materials and structures*, pp. 323–372, San Diego, CA: Academic Press, 1999.
- [7] M. Sargent III, M. O. Scully, and J. E. Lamb, *Laser physics*. Massachusetts: Addison-Wesley, 1974.
- [8] J. D. Jackson, *Classical electrodynamics*. New York: Wiley, 1975.
- [9] C. W. Gardiner, *Quantum noise*. Berlin: Springer-Verlag, 1991.
- [10] H. F. Hofmann, *Quantum noise and spontaneous emission in semiconductor laser devices*. PhD dissertation, Institut für Technische Physik, 1999.
- [11] C. W. Gardiner, *Handbook of stochastic methods. 2nd Ed.* Berlin: Springer-Verlag, 1995.
- [12] M. San Miguel and R. Toral, “Stochastic effects in physical systems,” *Procs. of instabilities and non-equilibrium structures VI*, p. 35, Dordrecht: Kluwer academic, 2000.

- [13] M. San Miguel, Q. Feng, and J. V. Moloney, "Light-polarization dynamics in surface-emitting semiconductor lasers," *Phys. Rev. A*, vol. 52, no. 2, pp. 1728–1739, 1995.
- [14] K. Panajotov, B. Ryvkin, J. Danckaert, M. Peeters, H. Thienpont, and I. Veretennicoff, "Polarization switching in VCSELs due to thermal lensing," *IEEE Photonics Technol. Lett.*, vol. 10, no. 1, pp. 6–8, 1998.
- [15] M. P. van Exter, A. K. J. van Doorn, and J. P. Woerdman, "Electro-optic effect and birefringence in vertical-cavity surface-emitting lasers," *Phys. Rev. A*, vol. 56, pp. 845–853, 1997.
- [16] A. K. J. van Doorn, M. P. van Exter, and J. P. Woerdman, "Elasto-optic anisotropy and polarization orientation of vertical-cavity surface-emitting semiconductor lasers," *Appl. Phys. Lett.*, vol. 69, pp. 1041–1043, 1996.
- [17] D. Burak, J. V. Moloney, and R. Binder, "Microscopic theory of polarization properties of optically anisotropic vertical-cavity surface-emitting lasers," *Phys. Rev. A*, vol. 61, p. 053809, 2000.
- [18] K. Panajotov, B. Nagler, G. Verschaffelt, A. Georgievski, H. Thienpont, J. Danckaert, and I. Veretennicoff, "Impact of in-plane anisotropic strain on the polarization behavior of vertical-cavity surface-emitting lasers," *Appl. Phys. Lett.*, vol. 77, pp. 1590–1592, 2000.
- [19] L. Viña, "Spin relaxation rate in low-dimensional systems," *J. Phys.: Condens. Matter*, vol. 11, pp. 5929–5952, 1999.
- [20] A. Tackeuchi, T. Kuroda, S. Muto, Y. Nishikawa, and O. Wada, "Electron spin-relaxation dynamics in GaAs/AlGaAs quantum wells and InGaAs/InP quantum wells," *Jpn. J. Appl. Phys.*, vol. 38, no. 8, pp. 4680–4687, 1999.
- [21] H. Ando, T. Sogawa, and H. Gotoh, "Photon-spin controlled lasing oscillation in surface-emitting lasers," *Appl. Phys. Lett.*, vol. 73, no. 5, pp. 566–568, 1998.
- [22] G. P. Agrawal and C. M. Bowden, "Concept of linewidth enhancement factor in semiconductor lasers: Its usefulness and limitations," *IEEE Photonics Technol. Lett.*, vol. 5, no. 6, pp. 640–642, 1993.
- [23] A. Valle and L. Pesquera, "Relative intensity noise of multitransverse mode vertical-cavity surface-emitting lasers," *IEEE Photonics Technol. Lett.*, vol. 13, no. 4, pp. 272–274, 2001.
- [24] M. San Miguel, "Polarization properties of vertical-cavity surface-emitting lasers," In *Semiconductor Quantum Optoelectronics*, p. 339, Bristol: Institute of Physics, 1999.

- [25] J. Martín-Regalado, F. Prati, M. San Miguel, and N. Abraham, "Polarization properties of vertical-cavity surface-emitting lasers," *IEEE J. Quantum Electron.*, vol. 33, no. 5, pp. 765–783, 1997.
- [26] J. Martín-Regalado, J. L. Chilla, J. J. Rocca, and P. Brusenbach, "Polarization switching in vertical-cavity surface emitting lasers observed at constant active region temperature," *Appl. Phys. Lett.*, vol. 70, no. 25, pp. 3350–3352, 1997.
- [27] K. D. Choquette, D. A. Richie, and R. E. Leibenguth, "Temperature dependence of gain-guided vertical-cavity surface emitting laser polarization," *Appl. Phys. Lett.*, vol. 64, no. 16, pp. 2062–2064, 1994.
- [28] B. Ryvkin, K. Panajotov, A. Georgievski, J. Danckaert, M. Peeters, G. Verschaffelt, H. Thienpont, and I. Veretennicoff, "Effect of photon-energy-dependent loss and gain mechanisms on polarization switching in vertical-cavity surface-emitting lasers," *J. Opt. Soc. Am. B*, vol. 16, no. 11, pp. 2106–2113, 1999.
- [29] S. Balle, E. Tolkachova, M. San Miguel, J. Tredicce, J. Martín-Regalado, and A. Gahl, "Mechanisms of polarization switching in single-transverse-mode vertical-cavity surface-emitting lasers: thermal shift and nonlinear semiconductor dynamics," *Opt. Lett.*, vol. 24, no. 16, pp. 1121–1123, 1999.
- [30] M. San Miguel, S. Balle, J. Mulet, C. R. Mirasso, E. Tolkachova, and J. R. Tredicce, "Combined effects of semiconductor gain dynamics, spin dynamics and thermal shift in polarization selection in VCSELs," *Proc. SPIE*, vol. 3944, pp. 242–251, 2000.
- [31] G. P. Agrawal, "Mode-partition noise and intensity correlation in a two-mode semiconductor laser," *Phys. Rev. A*, vol. 37, no. 7, pp. 2488–2494, 1988.
- [32] F. Koyama, K. Morito, and K. Iga, "Intensity noise and polarization stability of GaAlAs-GaAs surface emitting lasers," *IEEE J. Quantum Electron.*, vol. 27, no. 6, pp. 1410–1416, 1991.
- [33] K. H. Hahn, M. R. Tan, and S.-Y. Wang, "Intensity noise of large area vertical cavity surface emitting lasers in multimode optical fibre links," *Electron. Lett.*, vol. 30, no. 2, pp. 139–140, 1994.
- [34] D. V. Kuksenkov, H. Temkin, and S. Swirhun, "Polarization instability and relative intensity noise in vertical cavity surface emitting lasers," *Appl. Phys. Lett.*, vol. 67, no. 15, pp. 2141–2143, 1995.

- [35] D. C. Kilper, P. A. Roos, J. L. Carlsten, and K. L. Lear, "Squeezed light generated by a microcavity laser," *Phys. Rev. A*, vol. 55, no. 5, pp. R3323–R3326, 1997.
- [36] J.-L. Vey and W. Elsässer, "Semiclassical description of noise and generation of amplitude squeezed states with vertical cavity surface-emitting semiconductor lasers," *J. Opt. Soc. Am. B*, vol. 14, no. 6, pp. 1299–1304, 1997.
- [37] J.-L. Vey and W. Elsässer, "Noise and amplitude-squeezing performance of two polarization-mode semiconductor lasers," *Opt. Lett.*, vol. 23, no. 9, pp. 721–723, 1998.
- [38] F. Marin and G. Giacomelli, "Polarization and transverse mode dynamics in VCSELs," *J. Opt. Soc. Am. B*, vol. 1, no. 1, pp. 128–132, 1999.
- [39] G. Giacomelli, F. Marin, M. Gabrysch, K. H. Gulden, and M. Moser, "Polarization competition and noise properties of VCSELs," *Opt. Comm.*, vol. 146, no. 1, pp. 136–140, 1998.
- [40] J.-P. Hermier, A. Bramati, A. Z. Khoury, E. Giacobino, J.-P. Poizat, T. J. Chang, and P. Grangier, "Spatial quantum noise of semiconductor lasers," *J. Opt. Soc. Am. B*, vol. 16, no. 11, pp. 2140–2146, 1999.
- [41] J. P. Hermier, A. Bramati, A. Z. Khoury, V. Josse, E. Giacobino, P. Schnitzer, R. Michalzik, and K. J. Ebeling, "Noise characteristics of oxide-confined vertical-cavity surface-emitting lasers," *IEEE J. Quantum Electron.*, vol. 37, no. 1, pp. 87–91, 2001.
- [42] A. Valle, J. Sarma, and K. A. Shore, "Spatial holeburning effects on the dynamics of vertical cavity surface-emitting laser diodes," *IEEE J. Quantum Electron.*, vol. 31, no. 8, pp. 1423–1431, 1995.
- [43] A. Valle and L. Pesquera, "Mode partition noise in multi-transverse mode vertical-cavity surface-emitting lasers," *Proc. SPIE*, vol. 3625, p. 46, 1999.
- [44] J. Y. Law and G. P. Agrawal, "Mode-partition noise in vertical-cavity surface-emitting lasers," *IEEE Photonics Technol. Lett.*, vol. 9, no. 4, pp. 437–439, 1997.
- [45] K. J. Ebeling, "Analysis of vertical-cavity surface-emitting lasers diodes (VCSELs)," In *Semiconductor Quantum Optoelectronics*, p. 295, Bristol: Institute of Physics, 1999.
- [46] M. P. van Exter, M. B. Willemsen, and J. P. Woerdman, "Characterizing and understanding VCSEL polarization noise," *Proc. SPIE*, vol. 3946, pp. 58–68, 2000.

- [47] M. P. van Exter, M. B. Willemsen, and J. P. Woerdman, "Polarization fluctuations in vertical-cavity semiconductor lasers," *Phys. Rev. A*, vol. 58, no. 5, pp. 4191–4205, 1998.
- [48] M. P. van Exter, A. Al-Remawi, and J. P. Woerdman, "Polarization fluctuations demonstrate nonlinear anisotropy of a vertical-cavity semiconductor laser," *Phys. Rev. Lett.*, vol. 80, no. 22, pp. 4875–4878, 1998.
- [49] M. B. Willemsen, M. P. van Exter, and J. P. Woerdman, "Correlated fluctuations in the polarization modes of a vertical-cavity semiconductor laser," *Phys. Rev. A*, vol. 60, no. 5, pp. 4105–4113, 1999.
- [50] E. Goodbar, J. W. Scott, B. Thibeault, G. Robinson, Y. Akulova, and L. A. Coldren, "Calibrated intensity noise measurements in microcavity laser diodes," *Appl. Phys. Lett.*, vol. 67, no. 25, pp. 3697–3699, 1995.
- [51] C. Degen, J.-L. Vey, P. Schnitzer, and K. J. Ebeling, "Amplitude noise squeezed light from polarization singlemode VCSEL," *Electron. Lett.*, vol. 34, no. 16, pp. 1585–1587, 1998.
- [52] M. P. van Exter, M. B. Willemsen, and J. P. Woerdman, "Effect of mode-partition noise on intensity squeezing in a two-mode laser," *J. Opt. Soc. Am. B*, vol. 1, no. 6, pp. 637–645, 1999.
- [53] T. Erneux, J. Danckaert, K. Panajotov, and I. Veretennicoff, "Two-variable reduction of the San Miguel-Feng-Moloney model for vertical-cavity surface-emitting lasers," *Phys. Rev. A*, vol. 59, no. 6, pp. 4660–4667, 1999.
- [54] M. B. Willemsen, M. P. van Exter, and J. P. Woerdman, "Anatomy of a polarization switch of a vertical-cavity semiconductor laser," *Phys. Rev. Lett.*, vol. 84, no. 19, pp. 4337–4340, 2000.
- [55] M. Giudici, T. Ackemann, S. Barland, J. Tredicce, and S. Balle, "Polarization dynamics in vertical-cavity surface-emitting lasers with optical feedback: experiment and model," *J. Opt. Soc. Am. B*, vol. 16, no. 11, pp. 2114–2123, 1999.
- [56] J.-P. Hermier, I. Maurin, A. Bramati, A. Z. Khoury, and E. Giacobino, "Quantum spin flip model for vertical-cavity surface-emitting lasers." Poster CLEO-EQEC Nice, France, 2000.
- [57] J. Martín-Regalado, *Polarization properties of vertical-cavity surface-emitting lasers*. PhD dissertation, Universitat de les Illes Balears, 1997. Online access <http://www.imedeia.uib.es/publicationsdbfiles/000280/>
- [58] H. van der Lem and D. Lenstra, "Saturation-induced frequency shift in the noise spectrum of a birefringent vertical-cavity surface-emitting laser," *Opt. Lett.*, vol. 22, pp. 1698–1700, 1997.

-
- [59] R. F. M. Hendriks, M. P. van Exter, J. P. Woerdman, L. Weegels, and A. Van Geelen, "Polarization noise in elliptically polarized vertical-cavity surface-emitting lasers," *J. Opt. Soc. Am. B*, vol. 16, no. 5, pp. 832–834, 1999.
- [60] S. Ciuchi, M. San Miguel, and N. B. Abraham, "Polarization partition noise and intensity fluctuation linewidth in a nearly symmetric vector laser," *Phys. Rev. A*, vol. 57, no. 5, pp. 3843–3857, 1998.
- [61] J.-L. Vey, C. Degen, K. Auen, and W. Elsässer, "Quantum noise and polarization properties of vertical-cavity surface-emitting lasers," *Phys. Rev. A*, vol. 60, no. 4, pp. 3284–3295, 1999.
- [62] S. Balle, "Simple analytical approximations for the gain and refractive index spectra in quantum-well lasers," *Phys. Rev. A*, vol. 57, pp. 1304–1312, 1998.
- [63] J. Mulet, S. Balle, M. San Miguel, and C. R. Mirasso, "Transverse and polarization mode selection in vertical-cavity surface-emitting lasers," *IEEE 17th International Semiconductor Laser Conference*, pp. 101–102, 2000.
- [64] J. Mulet and S. Balle, "Modeling large-signal polarization and transverse dynamics in VCSELs," *Accepted in IEEE J. Quantum Electron.*, 2001.

CURRICULUM VITAE

Josep Mulet Pol

Información Personal

Nombre : José Mulet Pol
Fecha de nacimiento: 20/1/1975
Localidad : Lloseta
Provincia : Baleares
Nacionalidad : Española
Estado civil : Soltero
NIF : 78215109-K
Dirección : C./ Antoni Oliver 2, E-07360 Lloseta (Baleares)
e-mail : mulet@imedea.uib.es
URL : <http://www.imedea.uib.es/~mulet>

Educación¹

1981 - 1989 Enseñanza General Básica
La Salle, Inca (Baleares)
1989 - 1993 Bachillerato y COU
I.B. Berenguer d'Anoia, Inca (Baleares)
1993 - 1998 Licenciatura en ciencias Físicas
Universitat de les Illes Balears, Palma (Baleares)
Convocatoria de junio, con nota media de 2,7.
1998 - 1999 Curs d'adaptació pedagògica CAP
ICE Palma (Balears). Calificación: excelente

Becas concedidas

- I. Beca de colaboración del Ministerio de Educación y Cultura, durante el período comprendido 10/11/97 - 30/6/98. Grupo de fotónica del dept. de Física de la Universidad de las Islas Baleares (UIB).
- II. Beca Predoctoral. Subprograma de formación de profesorado universitario. Resolución BOE 19/1/1999. Centro de aplicación: Dept. Física Interdisciplinar. Instituto Mediterráneo de Estudios Avanzados (IMEDEA), CSIC-UIB.

¹El baremo utilizado es 1=Aprovado, 2=Notable, 3=Sobresaliente, 4=Matrícula de honor.

Idiomas

Conocimiento tanto oral como escrito de las lenguas Catalana, Castellana e Inglesa.

Cursos de especialización

Cursos de doctorado en la Universitat de les Illes Balears

- *Sistemas dinámicos*. O. Piro, E. Hernández. UIB 1999 [3 créditos]
- *Dinámica de estructuras espacio temporales*. E. Hernández, O. Piro, y M. San Miguel. UIB 2000 [5 créditos]
- *Sistemas de comunicaciones ópticas*. C.R. Mirasso. UIB 2000 [3 créditos]
- *Óptica cuántica*. P. Colet y G. Izús. UIB 2000 [3 créditos]

Cursos de doctorado en la Universidad de Cantabria. Convenio UC-UIB

- *Física y dinámica no lineal de láseres*. R.Vilaseca, P. Colet. Santander (1999) [3 créditos]
- *Láseres de pozo cuántico*. I. Esquivas. Santander (1999) [3 créditos]
- *Láseres para comunicaciones ópticas*. S. Balle. Santander (1999) [3 créditos]

Cursos en el extranjero

- *International summer school on semiconductor lasers*. 25-30 Julio 1999. Cork (Irlanda). J. McInerney, S. Koch, W. Chow, P. Blood, J.V. Moloney.

Estancias breves en centros de investigación

- Institute of Applied Physics, Darmstadt University of Technology. Darmstadt, (Alemania). Acciones integradas hispano-alemanas. Bajo supervisión de Dr. I. Fischer (19-24 Abril 1999).
- Department of computer & electrical engineering. Colorado State University, Fort Collins, CO (USA). Bajo supervisión de Dr. C. Menoni y Dr. J. Rocca. (1-10 Octubre 2000).
- Instituto de Física de Cantabria. Bajo supervisión de L. Pesquera y A. Valle. (9-13 Julio 2001).

Seminarios impartidos

- Transverse and Polarization Mode Selection in Vertical-Cavity Surface-Emitting Lasers. Thursday, 14 December 2000, Cross-Disciplinary Physics Department.

Presentaciones en congresos

- *Transverse and polarization mode dynamics in VCSELs.* J. Mulet, S. Balle, C.R. Mirasso, and M. San Miguel. CLEO/EQEC Focus Meeting 19-22 June 2001. Munich (Germany). Presentación: Oral.
- *Mesoscopic modelling of the transverse and polarization dynamics of VCSELs: Influence of thermal lensing.* J. Mulet, S. Balle, C.R. Mirasso, and M. San Miguel. VISTA meeting 11-13 June 2001. Paris (France). Presentación: Oral.
- *Transverse and polarization mode selection in VCSELs.* J. Mulet, C. R. Mirasso, S. Balle and M. San Miguel. Physics and simulation of optoelectronic devices IX. San José (USA) (2001). Presentación: Oral.
- *Dynamical behavior of two distant mutually coupled semiconductor lasers.* J. Mulet, C.R. Mirasso, T. Heil and I. Fischer. Physics and simulation of optoelectronic devices IX, San José (USA) (2001). Presentación: Oral.
- *Transverse and polarization mode selection in VCSELs.* J. Mulet, S. Balle, M. San Miguel, and C.R. Mirasso. 17th IEEE International semiconductor laser conference, 25-28 September 2000 Monterey, CA (USA). Presentación: Poster.
- *Transverse and polarization mode selection in VCSELs.* J. Mulet, S. Balle, C.R. Mirasso, M. San Miguel, E. Tolkachova and J.R. Tredicce. Conference on lasers and electro-optics Europe CLEO/IQEC, Nice Acropolis (France) 10-15 September 2000. Presentación: Oral.
- *Dynamical behavior of mutually-coupled semiconductor lasers: modelling and simulations.* J. Mulet, C.R. Mirasso, T. Heil, and I. Fischer. Conference on lasers and electro-optics Europe CLEO/IQEC, Nice Acropolis (France) 10-15 September 2000. Presentación: Poster.
- *Dynamical behavior of mutually coupled semiconductor lasers: Experimental Investigations.* T. Heil, I. Fischer, W. Elssasser, J. Mulet, and C.R. Mirasso. Conference on lasers and electro-optics Europe CLEO/IQEC, Nice Acropolis (France) 10-15 September 2000. Presentación: Oral.

- *Transverse and polarization mode selection in VCSELs.* J. Mulet, S. Balle, C.R. Mirasso and M. San Miguel. COST 268 & European VCSEL workshop, 28-30 August 2000, Brussels (Belgium). Presentación: Oral.
- *Intensity and polarization fluctuations in VCSELs.* J. Mulet, C.R. Mirasso, S. Balle and M. San Miguel. COST 268 & European VCSEL workshop, 28-30 August 2000, Brussels (Belgium). Presentación: Poster.
- *Fluctuations and Polarization Switching in VCSELs.* J. Mulet, C.R. Mirasso, S. Balle and M. San Miguel. Meeting of the TMR research network: *Microlasers and cavity QED*, 13-17 October 1999, Schloss Reisenburg (Germany). Presentación: Oral.
- *Intensity and Polarization fluctuations in VCSELs.* J. Mulet, C.R. Mirasso, and M. San Miguel. Quantum Optics X, 3-7 October 1999, Cala Vinyes (Mallorca). Presentación: Poster.
- *Numerical statistics of power dropouts in semiconductor lasers with optical feedback.* J. Mulet, C.R. Mirasso, T. Heil, and I. Fischer. Semiconductor Laser Workshop, El Escorial, Spain, 24-26 Sept. (1998). Presentación: Oral.
- *Low frequency fluctuations under single mode operation in DFB lasers.* T. Heil, J. Mulet, I. Fischer, and C.R. Mirasso. IEEE Lasers and Electro-Optics Society, Annual meeting Dec. 1998. Paper PD2.5. Presentación: Oral.

Publicaciones y Trabajos de investigación

- J. Mulet, C.R. Mirasso and M. San Miguel, “Polarization resolved intensity noise in VCSELs,” *Phys. Rev. A* **64**, 023817 (2001).
- T. Heil, I. Fischer, W. Elsasser, J. Mulet and C.R. Mirasso, “Chaos synchronization and spontaneous symmetry breaking in symmetrically delay coupled semiconductor lasers,” *Phys. Rev. Lett.* **86**, 795 (2001).
- J. Mulet, C.R. Mirasso, S. Balle and M. San Miguel, “Transverse and polarization mode selection in VCSELs,” *Proc. of SPIE* **4283**, 139 (2001).
- J. Mulet, C.R. Mirasso, T. Heil and I. Fischer, “Dynamical behavior of two distant mutually coupled semiconductor lasers,” *Proc. of SPIE* **4283**, 293 (2001).
- J. Mulet and S. Balle, “Modeling large-signal transverse and polarization dynamics in VCSELs,” Accepted in *IEEE J. Quantum Electron.* (2001).

- J. Mulet, C.R. Mirasso, S. Balle and M. San Miguel, “*Transverse mode dynamics in gain-switched vertical-cavity surface-emitting lasers*,” Submitted to IEEE Photon. Technol. Lett. (2001).
- C.R. Mirasso, J. Mulet, and C. Masoller, “*Chaos shift keying encryption in chaotic external-cavity semiconductor lasers using a single receiver scheme*,” Submitted to IEEE Photon. Technol. Lett. (2001).
- A. Scire, J. Mulet, C.R. Mirasso and M. San Miguel, “*Intensity and polarization selfpulsations in VCSELs*,” Submitted to Opt. Lett. (2001).
- M. San Miguel, S. Balle, J. Mulet, C.R. Mirasso, E. Tolkachova, and J.R. Tredicce, “*Combined effects of semiconductor gain dynamics, spin dynamics and thermal shift in polarization selection in VCSELs*,” Proc. of SPIE **3944**, 242 (2000).
- T. Heil, J. Mulet, I. Fischer, W. Elsasser and C.R. Mirasso, “*Statistical Properties of low frequency fluctuations under single mode operation in DFB lasers: Experiments and modelling*,” Opt. Lett. **24**, 1275 (1999).
- J. Mulet and C. R. Mirasso, “*Numerical Statistics of power dropouts based on the Lang-Kobayashi model*”, Phys. Rev. E **59**, 5400 (1999).
- Tesina de Licenciatura: Josep Mulet Pol, “*Statistics of Power Dropouts in Semiconductor Lasers with Optical Feedback and Current Modulation*”. UIB Setiembre 1998. Calificación: excelente.

Otros méritos

- Capacidad de manejo de sistemas operativos DOS, WINDOWS 9x’, UNIX, LINUX. Conocimiento de programación en diversos lenguajes: FORTRAN, BASIC, IDL, HTML, \LaTeX ...
- Desarrollo de un programa con interface gráfica que simula la dinámica del láser de semiconductor con retro-alimentación óptica (1997-1998).
- Premio extraordinario de licenciatura en ciencias Físicas. Curso académico 1997/1998 (FOU n. 161, 29 Abril de 1999).